Variable cell growth yields reproducible organ development through spatiotemporal averaging

Lilan Hong, Mathilde Dumond, Satoru Tsugawa, Aleksandra Sapala, Anne-Lise Routier-Kierzkowska, Yong Zhou, Catherine Chen, Annamaria Kiss, Mingyuan Zhu, Olivier O. Hamant, et al.

▶ **To cite this version:**

Lilan Hong, Mathilde Dumond, Satoru Tsugawa, Aleksandra Sapala, Anne-Lise Routier-Kierzkowska, et al.. Variable cell growth yields reproducible organ development through spatiotemporal averaging. Developmental Cell, 2016, 38 (1), pp.15-32. 10.1016/j.devcel.2016.06.016 . hal-02635442

HAL Id: hal-02635442
https://hal.inrae.fr/hal-02635442v1

Submitted on 20 Jan 2024

HAL is a multi-disciplinary open access archive for the deposit and dissemination of scientific research documents, whether they are published or not. The documents may come from teaching and research institutions in France or abroad, or from public or private research centers.

L'archive ouverte pluridisciplinaire **HAL**, est destinée au dépôt et à la diffusion de documents scientifiques de niveau recherche, publiés ou non, émanant des établissements d'enseignement et de recherche français ou étrangers, des laboratoires publics ou privés.

Article

Developmental Cell

Variable Cell Growth Yields Reproducible Organ Development through Spatiotemporal Averaging

Graphical Abstract

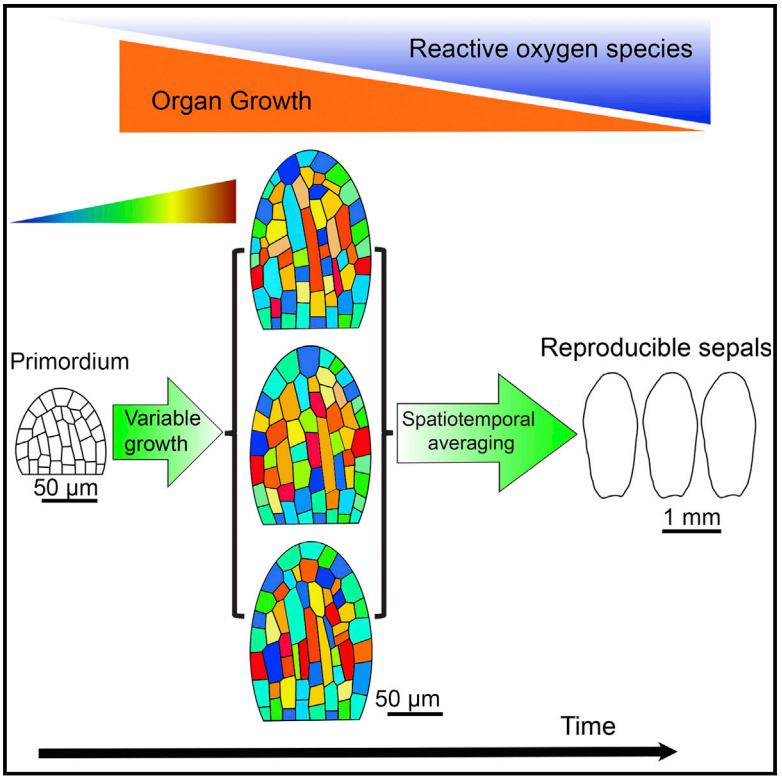

Authors

Lilan Hong, Mathilde Dumond, Satoru Tsugawa, ..., Chun-Biu Li, Arezki Boudaoud, Adrienne H.K. Roeder

Correspondence

arezki.boudaoud@ens-lyon.fr (A.B.), ahr75@cornell.edu (A.H.K.R.)

In Brief

During development, organs form with reproducible sizes and shapes despite the variable and unpredictable growth of their cells. Through live imaging and computational modeling of *Arabidopsis* sepals, Hong et al. show that spatiotemporal averaging of cellular variability resolves this apparent contradiction. Reactive oxygen species inhibit spatiotemporal averaging and promote organ maturation.

Highlights

- Reduced cellular variability can lead to the formation of irregular organs
- Spatiotemporal averaging of noisy cellular growth produces uniform organs
- Reactive oxygen species (ROS) promote maturation of sepals
- Abnormal ROS accumulation hinders the averaging of noisy cellular growth

Hong et al., 2016, Developmental Cell *38*, 15–32
July 11, 2016 © 2016 Elsevier Inc.
http://dx.doi.org/10.1016/j.devcel.2016.06.016

CellPress

Developmental Cell
Article

Variable Cell Growth Yields Reproducible Organ Development through Spatiotemporal Averaging

Lilan Hong,[1,6] Mathilde Dumond,[2,5,6] Satoru Tsugawa,[3,6] Aleksandra Sapala,[4] Anne-Lise Routier-Kierzkowska,[4] Yong Zhou,[1,7] Catherine Chen,[1] Annamaria Kiss,[2,5] Mingyuan Zhu,[1] Olivier Hamant,[2,5] Richard S. Smith,[4] Tamiki Komatsuzaki,[3] Chun-Biu Li,[3] Arezki Boudaoud,[2,5,*] and Adrienne H.K. Roeder[1,*]

[1]Weill Institute for Cell and Molecular Biology and Section of Plant Biology, School of Integrative Plant Sciences, Cornell University, Ithaca, NY 14853, USA

[2]Laboratoire de Reproduction et Développement des Plantes, Université de Lyon, ENS de Lyon, UCBL, INRA, CNRS, 46 Allée d'Italie, 69364 Lyon Cedex 07, France

[3]Research Institute for Electronic Science, Hokkaido University, Kita 20 Nishi 10, Kita-ku, Sapporo 001-0020, Japan

[4]Department of Comparative Development and Genetics, Max Planck Institute for Plant Breeding Research, Carl-von-Linné-Weg 10, 50829 Köln, Germany

[5]Laboratoire Joliot Curie, CNRS, ENS de Lyon, Université de Lyon, 46 Allée d'Italie, 69364 Lyon Cedex 07, France

[6]Co-first author

[7]Present address: Agricultural College, Yangzhou University, Yangzhou 225009, P.R. China

*Correspondence: arezki.boudaoud@ens-lyon.fr (A.B.), ahr75@cornell.edu (A.H.K.R.)

http://dx.doi.org/10.1016/j.devcel.2016.06.016

SUMMARY

Organ sizes and shapes are strikingly reproducible, despite the variable growth and division of individual cells within them. To reveal which mechanisms enable this precision, we designed a screen for disrupted sepal size and shape uniformity in *Arabidopsis* and identified mutations in the mitochondrial i-AAA protease FtsH4. Counterintuitively, through live imaging we observed that variability of neighboring cell growth was reduced in *ftsh4* sepals. We found that regular organ shape results from spatiotemporal averaging of the cellular variability in wild-type sepals, which is disrupted in the less-variable cells of *ftsh4* mutants. We also found that abnormal, increased accumulation of reactive oxygen species (ROS) in *ftsh4* mutants disrupts organ size consistency. In wild-type sepals, ROS accumulate in maturing cells and limit organ growth, suggesting that ROS are endogenous signals promoting termination of growth. Our results demonstrate that spatiotemporal averaging of cellular variability is required for precision in organ size.

INTRODUCTION

Developmental robustness is the ability of an organism to produce the same phenotype regardless of perturbations that occur; for instance, organisms can produce uniformly sized organs despite cellular variability. Within a species, the size of an organ is generally highly reproducible or precise (Lander, 2011). For example, brains of mice vary in size by only about 5% (Williams, 2000), the two arms of a person match in length with an accuracy of 0.2% (Wolpert, 2010), and *Arabidopsis* petals are strikingly uniform (Mizukami, 2001). However, the behavior of cells that make up organs is often variable and unpredictable (Doupé et al., 2010; Gupta et al., 2011; Meyer and Roeder, 2014; Singh et al., 2013). Equivalent neighboring plant cells grow at markedly different rates in several developing tissues (Armour et al., 2015; Elsner et al., 2012; Kierzkowski et al., 2012; Tauriello et al., 2015; Uyttewaal et al., 2012), although at later stages of development, growth may become more uniform (Zhang et al., 2011). Similarly, neighboring cells have different constriction rates during *Drosophila* gastrulation (Martin et al., 2009). Thus, how robust organ sizes emerge from the variable growth of cells is a central question in biology.

Although signaling pathways regulating organ size and shape have been identified, the mechanism of robustness in size and shape has remained elusive. Screens for mutants with altered organ size have isolated mutants with defects in cell size, cell number, or both (Anastasiou et al., 2007; Andriankaja et al., 2012; Deprost et al., 2007; Dinneny et al., 2004; Disch et al., 2006; Horiguchi et al., 2005; Karidas et al., 2015; Kawade et al., 2013; Kim and Kende, 2004; Mizukami and Fischer, 2000; Montagne et al., 1999; Nath et al., 2003; Ohno et al., 2004; Palatnik et al., 2003; Powell and Lenhard, 2012; Ren et al., 2011; Sauret-Güeto et al., 2013; Tumaneng et al., 2012; White, 2006). Although these mutants produce larger or smaller organs, they still tend to produce organs that all have the same size within the same genotype, and thus have little or no effect on robustness. Similarly, mutants disrupting organ shape have been isolated (Cui et al., 2010; Green et al., 2010; Nath et al., 2003; Sauret-Güeto et al., 2013), but little is known about robustness of shape. Mutants with variable size and shape are needed to investigate the mechanism of robustness.

There is persuasive evidence that animals and plants ensure organ size robustness not simply by counting cells or assessing cell size, but by somehow monitoring the overall size of their organs (Day and Lawrence, 2000; Powell and Lenhard, 2012). Plant and animal organs with reduced cell divisions often undergo "compensation," whereby the cells enlarge to produce almost normally sized organs (Horiguchi and Tsukaya, 2011; Roeder et al., 2010). For example, plant leaves overexpressing a cyclin-dependent

kinase inhibitor have significantly reduced cell numbers yet still grow to relatively normal size through increased cell expansion (De Veylder et al., 2001; Ferjani et al., 2007; Hemerly et al., 1995; Kawade et al., 2010). Similarly, inhibition of cell division in *Drosophila* imaginal disks promotes cell enlargement to produce a normally sized wing (Colombani et al., 2012; Garelli et al., 2012; Neufeld et al., 1998; Vallejo et al., 2015; Weigmann et al., 1997). Nevertheless, how growing organs sense their size and know when to stop growth remains a mystery (Vogel, 2013).

Arabidopsis floral organs, particularly sepals, allow robustness in organogenesis to be assessed within a single plant. Each flower has four sepals with the same size; individual plants can produce more than 100 flowers, allowing a statistical assessment of organ size within an individual organism, which generally cannot be done in animals. Sepals are the outermost leaf-like floral organs, making them accessible for imaging throughout development. The consistent size and shape of sepals is required to enclose and protect the developing reproductive organs, maintaining an effective barrier against the external environment. In addition, the size of floral organs is relatively insensitive to environmental effects, allowing us to focus on intrinsic mechanisms. Finally, there is considerable variability in both cell growth and cell cycle within developing sepals (Qu et al., 2014; Roeder et al., 2010, 2012; Schiessl et al., 2012; Tauriello et al., 2015). Thus, sepals are a good model system for studying how robust organ size and shape arises from cellular variability.

Plant cells grow through the irreversible, turgor pressure-driven extension of their cell walls. These walls are composed of a polymer matrix of cellulose, hemicellulose, and pectins as well as heavily glycosylated proteins. Cellulose microfibrils are the major structural reinforcements and orient cellular growth (Cosgrove, 1993; Somerville et al., 2004). Pectins affect cell-wall stiffness, which is fairly heterogeneous within a cell and between cells, but is critical for the growth rate of cells and consequently for morphogenesis (Chebli et al., 2012; Milani et al., 2011; Peaucelle et al., 2011, 2008). Cell-wall stiffness inversely correlates with growth rates (Bassel et al., 2014; Milani et al., 2011). Computational modeling enables the prediction of morphogenesis from cell-wall mechanics, gene activity, or both (Boudon et al., 2015; Coen et al., 2004; Green et al., 2010; Kennaway et al., 2011; Kuchen et al., 2012; Roeder et al., 2011; Sassi et al., 2014; Sauret-Güeto et al., 2013).

In this study we have used molecular genetics, live imaging, and computational modeling to disentangle the links between cellular variability and organ precision. In contrast to previous mutant screens for increased or decreased average organ size, we screened for mutants that disrupted the robustness of sepal size and shape. We characterized the *variable organ size and shape 1* (*vos1*) mutant, ascribing its phenotype to the over-accumulation of reactive oxygen species (ROS). Our key conclusion is that spatiotemporal averaging of cellular variability promotes robustness in organ shape.

RESULTS

vos1 Mutants Have Increased Variability in Sepal Size and Shape

To investigate how plants maintain organ size and shape regularity, we screened for mutants with disrupted sepal uniformity within an individual plant and isolated a mutant that we named *variable organ size and shape 1* (*vos1*; Figure 1A). In this screen, we isolated six alleles of *vos1* (see Experimental Procedures), with similar phenotypes, indicating that this gene is essential for maintaining sepal uniformity. Wild-type *Arabidopsis* flowers have uniform sepal sizes (mean ± SD 1.23 ± 0.10 mm^2, n = 68, all four sepals from each flower were included in the analysis; Figures 1A, 1C, 1D, and S1D). In contrast, *vos1* mutants have sepals of different sizes within the same flower, failing to form an effective barrier to protect the inner developing reproductive organs (Figures 1A, 1C, 1D, and S1D). Thus, *vos1* sepals have a decreased average area and increased variance in area (Figure 1C; mean ± SD 0.85 ± 0.27 mm^2, n = 68, $p < 0.001$). Different *vos1* flowers from the same inflorescence also show great variability (Figures S1A and S1B).

Similarly, *vos1* sepals have irregular shapes (Figures 1A and S1B). We quantified variability in sepal shape (S_2), independent of size (Figure 1E; see Experimental Procedures). The median shape variability S_2 for *vos1* (median ± SE 0.0042 ± 0.0004, n = 518) was significantly increased compared with wild-type (median ± SE 0.0025 ± 0.0001, n = 215; Figure 1F).

In *vos1*, defects in organ regularity are also often observed in petals, stamens, carpels, and leaves (Figures 1A and S1A–S1C). We focus on the sepal phenotypes, which are representative of the defects seen in other organs.

To confirm that the decreased regularity in *vos1* sepals was not a concomitant effect of decreased sepal area, we analyzed the *kluh* (*klu*) mutant, which has smaller leaves (Anastasiou et al., 2007); *klu* sepals had smaller areas, but the variance in areas was indistinguishable from wild-type (Figures 1C, 1D, and S1D; mean ± SD 1.05 ± 0.13 mm^2, n = 67). Likewise, shape variability in *klu* sepal was similar to that in wild-type (Figures 1E and 1F; S_2 = 0.0026 ± 0.0003 [median ± SE], n = 66). We also examined a number of mutants known to affect organ size and did not observe any obvious decrease in sepal size uniformity (Figure S1E). Therefore, *vos1* mutants disrupt a distinct mechanism maintaining organ regularity, and loss of regularity is not a side effect of decreased organ size.

We next determined when during development the irregularity in *vos1* mutant sepals first occurs. In wild-type flowers, the sepal primordia became visible at stage 3 and grew to completely cover the bud at stage 6 (Figure 1B; Smyth et al., 1990). *vos1* sepals exhibited normal primordia at stages 3 and 4 (Figure 1B), indicating that the irregular sepals are not due to a defect in primordium initiation. The loss of sepal uniformity in *vos1* started to become visible at stage 5: some flowers had normal sepals, while others had irregular sepals (arrows in Figure 1B). Heterogeneity in shape intensified as *vos1* sepals grew. Gaps appeared between the *vos1* sepals, in contrast to the tightly closed sepals of wild-type flowers from stage 6 onward, suggesting that the *vos1* mutation affects the protective function of the sepals (Figure 1B).

Mechanical Modeling Shows that Spatiotemporal Averaging of Cellular Variability Can Produce Organ Regularity

Given previous observations that sepal cells are variable in growth and cell cycle (Roeder et al., 2010; Tauriello et al., 2015), we turned to computational modeling to understand the link between organ robustness and cellular variability and how

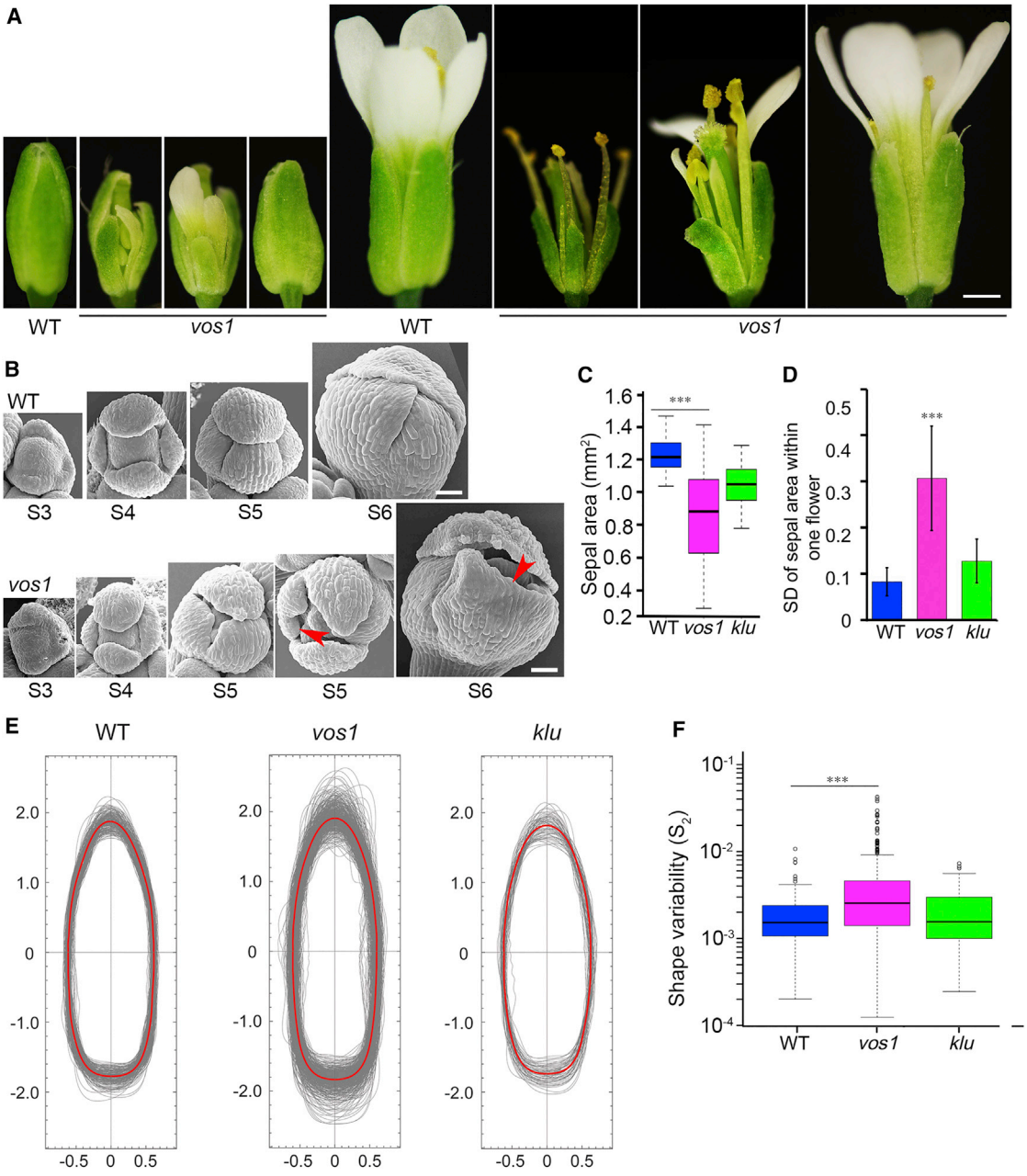

Figure 1. *vos1* Mutants Have Increased Variability in Sepal Size and Shape

(A) Wild-type (WT) and *vos1* flowers from single plants (some *vos1* with irregular sepals, some *vos1* with normal) before flower opening at stage 12 (left) and at maturity (stage 14; right).

(B) Scanning electron micrographs show that sepal primordia (stages 3–4 [S3–S4]) form normally in *vos1* mutants. The *vos1* sepal variability phenotype (arrowheads) starts at stage 5 (S5) and intensifies as the flower grows (S6–S7).

(C) Compared with WT, *vos1* has decreased median sepal area (stage 14) and increased variance in area. Not all organ size mutants show increased variability as exemplified by *klu*. ***$p < 0.001$, significant difference in variance from WT (f test). n = 68 for WT and *vos1*, n = 67 for *klu*.

(D) Mean SD of sepal area within one flower is increased in *vos1* compared with WT and *klu*. ***$p < 0.001$, significant difference in mean SD (t test), error bars representing the SD of the mean SD of the sepal area within one flower. n = 17 for WT and *vos1*, n = 14 for *klu*.

(E) *vos1* mutants have variable organ shape as well as size. Superimposed outlines of mature stage 14 sepals from WT, *vos1*, and *klu* were normalized by size to reveal differences in shape. The variation is the difference between the median outline (red) and that of the individual sepals (gray).

(F) Sepal shape variability S_2 (squared deviation of sepal outlines): *vos1* has increased sepal shape variance, while *klu* has sepal shape variance similar to that of WT. ***$p < 0.001$ (t test). n = 215 for WT, n = 518 for *vos1*, n = 66 for *klu* in (E) and (F).

For the boxplots, the box extends from the lower to upper quartile values of the data, with a line at the median, and the whiskers extend past 1.5 of the interquartile range. Scale bars represent 500 μm in (A) and 30 μm in (B). See also Figure S1.

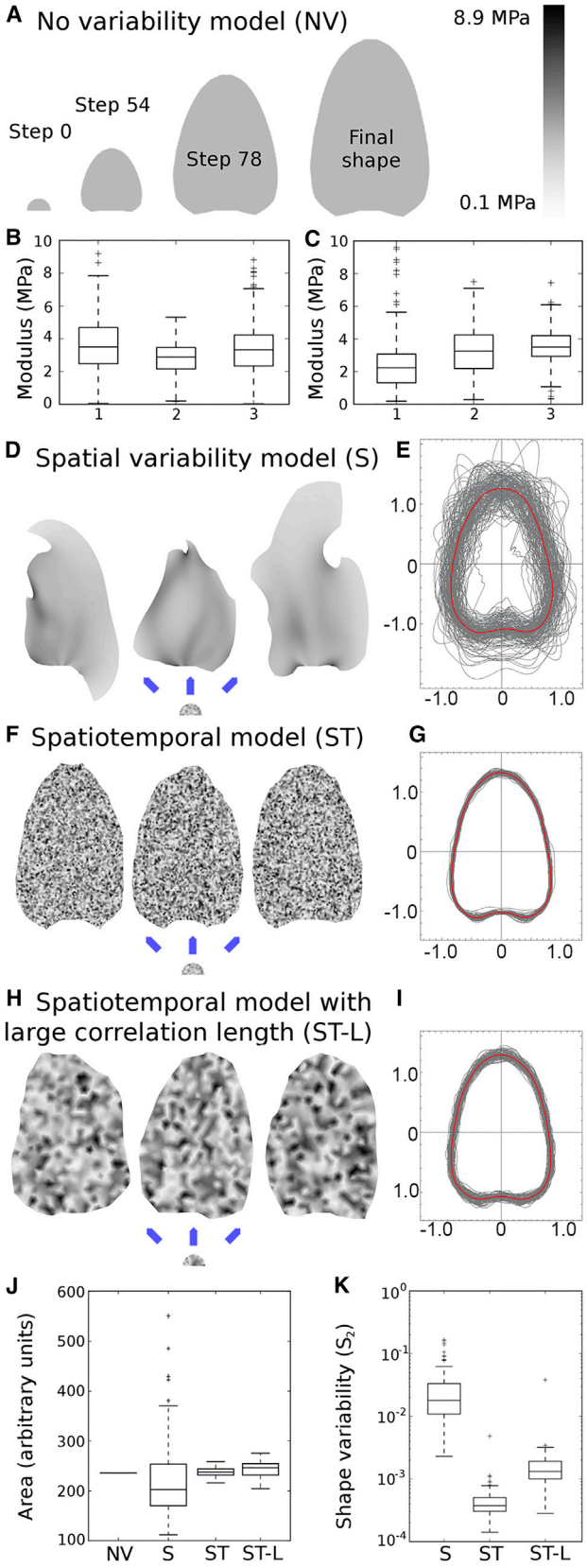

Figure 2. A Mechanical Model of Sepal Morphogenesis Predicts that Spatiotemporal Averaging of Local Variability in Growth Generates Robust Organ Shapes

(A) Examples of simulation steps of the model of sepal growth. A continuous, tissue-scale, mechanical model was implemented with transverse anisotropy in stiffness and with no variability of mechanical properties (NV).

(B and C) AFM measurements. Cell-wall mechanical properties are variable in the wild-type sepals (B) and the *vos1* sepals (C).

(D–K) Three models with variability in stiffness. Simulations are initialized from a half-disc-shaped sepal primordium shown below the simulated final states (D, F, H) with a random distribution of elastic moduli deduced from AFM. The modulus is represented by a grayscale heatmap: black is rigid, whereas white is flexible. (D) The spatial variability model (S) results in misshapen sepals. Stiffness persists throughout growth. Thus flexible regions (in light colors) grow protrusively while stiff areas (dark) grow little. Three replicates starting from different stiffness configurations in the primordium are shown. (E) Normalized outlines showing variability in shape for 140 simulations of type S. (F) Robust sepal shape arises from the spatiotemporal variability model (ST). At each time frame, each element selects a new stiffness from the probability distribution. Three replicates are shown. (G) Normalized outlines showing variability in shape for 100 simulations of type ST. (H) Sepal shapes are less robust with decreased local spatial variability (ST-L), i.e., when the correlation length is increased in the model otherwise identical to (F). This model mimics the decrease in local spatial variability (V_{area}) observed in *vos1* mutants (Figures 4D–4F). (I) Normalized outlines showing variability in shape for 100 simulations of type ST-L. (J) Simulated sepal area (a.u., initial area ~1) and (K) shape (S_2) variability with no variability (NV), spatial variability (S), spatiotemporal variability (ST), or spatiotemporal variability with a long correlation length (ST-L). Spatial variability alone leads to lack of robustness in final shape, while spatiotemporal variability yields more precise size (J) and shape (K). Longer correlation length leads to more variable sepals in size (J) and shape (K). The statistics are obtained over 100 replicates (simulation runs).

For the boxplots, the box extends from the lower to upper quartile values of the data, with a line at the median, and the whiskers extend past 1.5 of the interquartile range. See also Figure S2 and Movies S1, S2, S3, S4, and S5.

this link might be disrupted in *vos1* sepals. We built a continuous, tissue-scale, mechanical model of sepal growth (Figure 2A and Movie S1; see Experimental Procedures), as such models are sufficient to investigate how local regulation of growth determines organ shape (Coen et al., 2004; Green et al., 2010; Hervieux et al., 2016; Kennaway et al., 2011; Kuchen et al., 2012; Sauret-Güeto et al., 2013). We created a two-dimensional model because epidermal cells largely control the rate of growth in plant organs (Kutschera and Niklas, 2007; Savaldi-Goldstein et al., 2007).

In our mechanical model, we input variability in stiffness to mimic cellular heterogeneity of the tissue. To assign parameters, we measured the stiffness of wild-type sepal epidermal cells with atomic force microscopy (AFM) and found significant spatial variability in stiffness (Figures 2B, 2C, S2A, and S2B). In the model, organ growth ceased after the size reached a threshold (see Experimental Procedures). We first made a model with high spatial variability in stiffness of the sepal primordium based on our AFM data ("spatial variability model," S). Because in the model stiffness determined growth rate, softer regions grew more and stiffer regions grew less. All simulation runs produced misshapen organs, and size and shape were highly variable between the runs (Figures 2D and 2E; Movie S2). This suggested that some mechanism must mitigate spatial variability of individual cells for regularly sized organs to be possible.

In our next model, we maintained the spatial variability in stiffness, but allowed each region to randomly change stiffness in

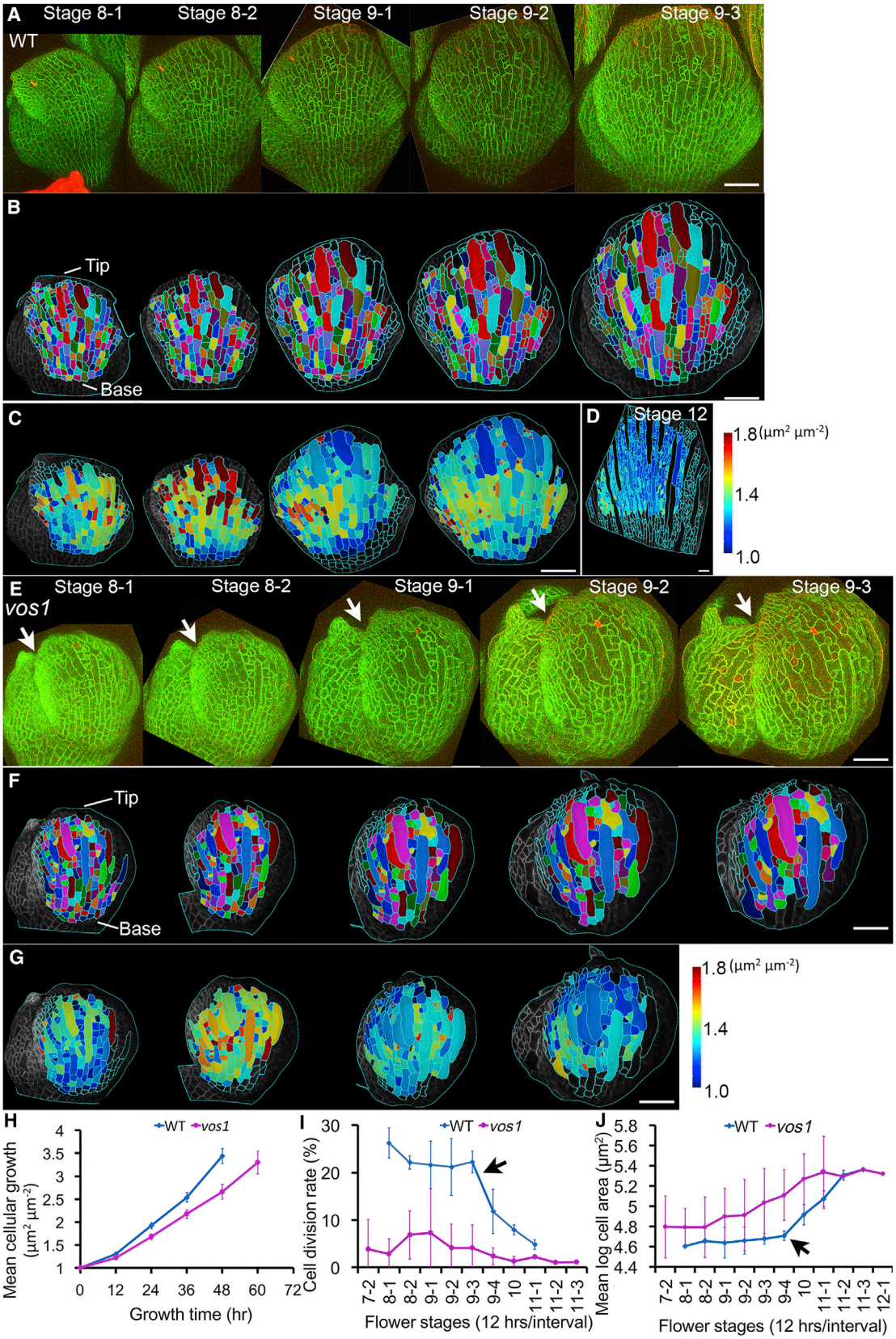

(legend on next page)

time ("spatiotemporal variability model," ST). In each time frame of the model, stiffness was randomly selected from the same distribution as in the first model. As the stiffness varied in space and time, the simulation produced correspondingly variable growth rates (Figures S2D and S2E); however, the spatiotemporal variability model generated sepals with regular sizes and shapes over all simulation runs (Figures 2F, 2G, 2J, and 2K; Movie S3). In essence, the temporal variability allowed the differences in stiffness to average in time; a high stiffness at one time was effectively counterbalanced by a low stiffness earlier or later in growth such that the sepal grew more like a model with uniform stiffness ("non-variable model," NV; Figures 2A and 2J; Movie S1). Likewise, a stiff spot next to a softer spot can somewhat counterbalance each other in growth. We call this combined phenomenon spatiotemporal averaging. We also explored models with intermediate levels of temporal variability and found that a relatively low temporal variability is sufficient to yield robust shapes (Figures S2C and S2G; Movie S4). Thus, although these initial models represent extreme cases (neither wild-type nor mutant), they demonstrate the fundamental principle that adding temporal variability over spatial variability produces regular organs through spatiotemporal averaging.

Reduced Local Spatial Variability in the Cell Growth of *vos1* Sepals Underlies Irregular Sepal Shape

Next, we tested whether defects in spatiotemporal averaging could explain the reduced regularity of *vos1* sepal shapes. To do so, we analyzed cell growth variability through live imaging of wild-type and *vos1* sepals (Cunha et al., 2012; Roeder et al., 2010). The same flower was imaged every 12 hrs (Figures 3A and 3E; arrows indicate gaps). We focused our analysis on the epidermis because epidermal cells largely control the rate of organ growth in plants (Kutschera and Niklas, 2007; Savaldi-Goldstein et al., 2007). MorphoGraphX software (Barbier de Reuille et al., 2015) was used to calculate growth rates and cell division rates (Figures 3B, 3F, and S3A–S3D; n = 405 cell lineages in wild-type sepals and 524 cell lineages in *vos1* mutant sepals; see Experimental Procedures). The sepal matures from tip to base (Hervieux et al., 2016; Roeder et al., 2010). Initially, the tip of the wild-type sepal had a high growth rate, then cell growth and cell division progressively slowed from the tip downward (Figures 3C and S3E). *vos1* mutant sepals also exhibited slower growth descending from tip to base as in wild-type (Figure 3G); however, growth rates decreased in *vos1* mutants more quickly than in wild-type (see below).

For spatiotemporal averaging to occur, growth of wild-type sepal cells should be variable in both time and space. We quantified the temporal variability in growth by calculating the change in a cell's growth (in area) between two consecutive 12-hr time intervals (D_{area}; Figures 4A and 4C; see Experimental Procedures). We quantified the local spatial variability in growth (in area) by calculating the differences in growth rates among neighboring cells (V_{area}; Figures 4D and 4F). For wild-type cells, the growth rate was highly variable in both space and time during stages 8–9 of sepal development (Figures 4A, 4C, 4D, and 4F). Thus, wild-type sepal cells exhibit both spatial and temporal variability in growth.

In contrast, local spatial growth variability (V_{area}) was substantially decreased in *vos1* mutants. The growth rate of each cell was more similar to its neighbors in *vos1* than in wild-type (V_{area} = 5.32% for *vos1* versus 7.69% in wild-type, $p < 10^{-6}$ [permutation test]; see Experimental Procedures; Figures 4E and 4F). Temporal variability in growth (D_{area}) of *vos1* cells partially overlapped with wild-type (D_{area} = 6.94% for *vos1* versus 8.37% for wild-type, $p < 10^{-6}$ [permutation test]; Figures 4B and 4C), suggesting that temporal variability in cell areal growth was only slightly altered in the *vos1* mutant. Therefore, contrary to our initial model, the *vos1* mutant sepal cells exhibit much less spatial variability and similar temporal variability in growth.

To understand the mechanistic basis for reduced spatial variability in *vos1*, we examined the local spatial variability in cell-wall stiffness of epidermal cells using AFM. In both wild-type and *vos1* sepals we observed subcellular variability in stiffness (Figure 4G). We quantified local stiffness variability (V_{AFM}) in a 35-by-35-μm square, by analogy with the calculation of V_{area} (see Experimental Procedures). Compared with wild-type, *vos1* had a substantial decrease in local spatial variability of stiffness (V_{AFM} = 37.3% for *vos1* versus 43.7% for wild-type, $p < 10^{-15}$ [t test]; Figure 4H). This result is consistent with the decreased local spatial variability in growth rates observed in *vos1*.

Our model prediction that reducing temporal variability produces irregular sepals does not explain our observations in *vos1*. Instead, the growth and AFM analysis in *vos1* suggest that the lower level of spatial variability inhibits sepal shape robustness, which we tested in our next model. Reducing local spatial variability means that neighboring cells are more correlated.

Figure 3. *vos1* Sepals Mature Earlier Than Wild-Type

(A and E) Confocal stack maximum-intensity projection images of wild-type (WT) (A) and *vos1* (E) flowers in which the epidermal cells are marked with a plasma membrane marker (green; *ATML1::mCitrine-RCI2A*). Arrows indicate the gaps between sepals that emerge in the mutant due to variability in sepal sizes. Flowers are staged based on their width. Each substage lasts for 12 hrs.

(B and F) WT (B) and *vos1* (F) sepals from images (A) and (E) are segmented into cells, and lineages are tracked with MorphoGraphX. Cells derived from the same mother cell at the starting time point are marked with the same color labels.

(C and G) Heatmap of the cellular areal growth rate in WT (C) and *vos1* (G) sepals. The growth rate is calculated as the ratio of the cell area at the later time point to the cell area at the earlier time point (displayed on the earlier time point).

(D) Heatmap of the cellular areal growth rate in a WT sepal at stage 12, which shows much lower growth rate compared with WT sepals at earlier stages.

(H) Average growth of cell areas calculated as the ratio with the cellular area at the starting time point. Each data point is mean ± SD. Total n = 705 for WT and n = 472 for *vos1*.

(I) Cell division rate represented by the percentage of cells that divide in the corresponding growth interval. Initially WT cell division rates are high, but decrease when the sepal matures (arrow), while *vos1* mutant division rates remain low.

(J) Average logarithmic areas of cells for developing sepals. Note that in WT, the average log area stays constant until the maturation phase when the average log area increases (arrow), while average log area increases throughout the mutant growth. n = 5 biological repeats for each genotype in (I) and (J), mean ± SD. Scale bars, 50 μm. See also Figure S3.

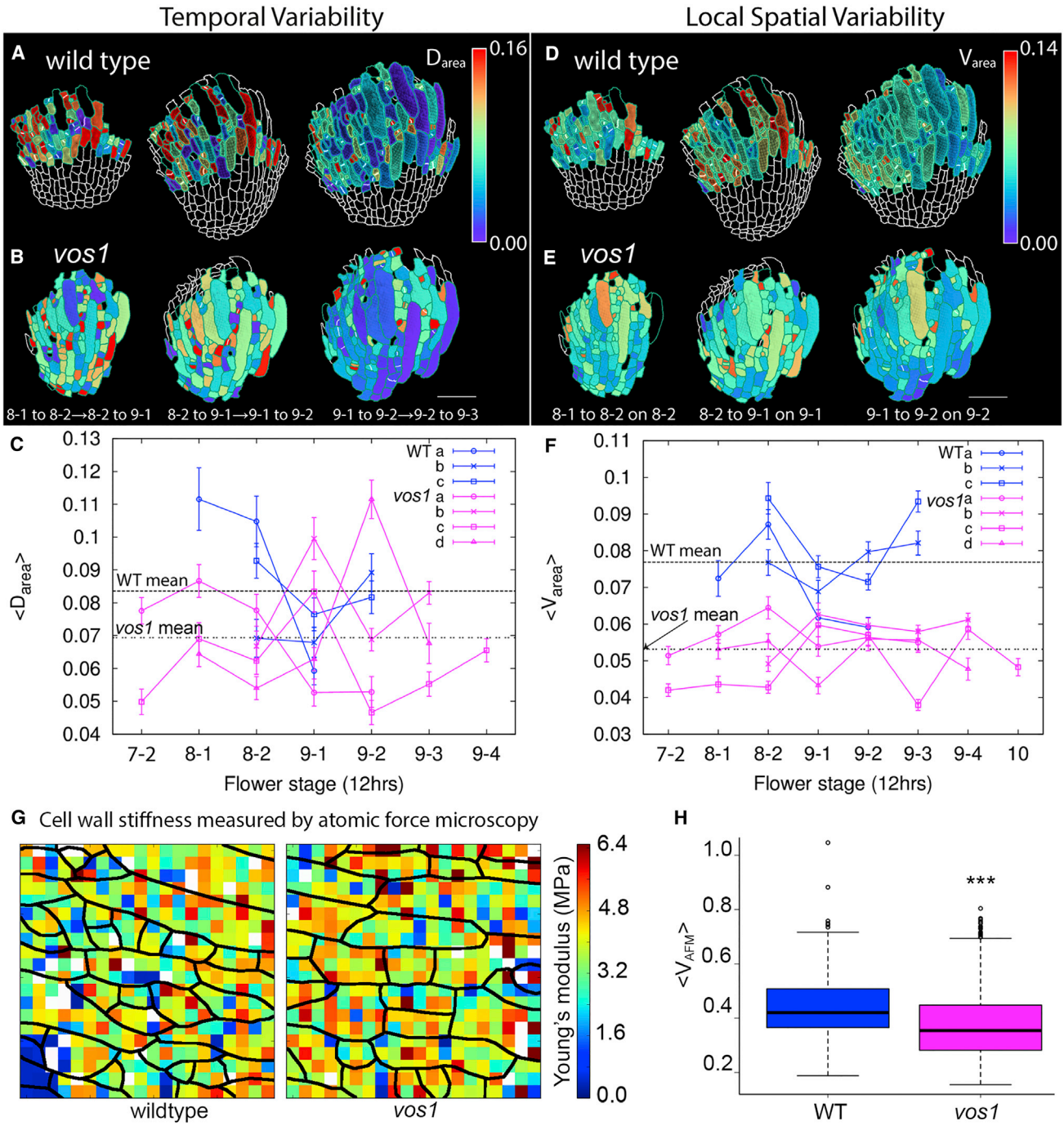

Figure 4. Spatial Variability of Cell Growth Rates in Area Is Decreased in *vos1*

(A–C) Temporal variation of the cell growth rate (D_{area}; heatmap with high variability in red and low variability in blue) is similar in wild-type (WT) and *vos1* sepals. Equivalent cells (defined by the proximity of differentiated stomata) outlined in green are analyzed for WT (A) and *vos1* (B) flowers at stages 8 and 9. Additional non-equivalent WT cells at the base of the sepal are outlined in white. Consecutive 12-hr growth intervals are analyzed; for example, 8-1 to 8-2 → 8-2 to 9-1 means that the growth rate during the 12-hr interval from stage 8-1 to 8-2 is compared with growth rate during the 12-hr interval from stage 8-2 to stage 9-1.

(C) Graph plotting the average temporal variability of the growth rates ($<D_{area}>$ signifies the average of D_{area} over cells) in each sepal epidermis at each time point. Three WT flowers (a–c, blue) and four *vos1* mutant flowers (a–d, magenta) are shown. Dotted black lines indicate the average temporal variability for all cells at all time points (WT 8.37%; *vos1* 6.94%). The WT and mutant data partially overlap and only slight differences of temporal variability ($<D_{area}>$) are detected ($p < 10^{-6}$, permutation test). The error bars represent the SE. Scale bar represents 50 μm.

(D–F) Local spatial variation in the cell growth rate (V_{area}; heatmap with high variability in red and low variability in blue) is decreased in *vos1* sepals. Flowers are the same as in (A)–(C). The 12-hr interval analyzed is specified by stages. For example, 8-1 to 8-2 on 8-2 is the 12-hr interval from stage 8-1 to stage 8-2 displayed on the sepal cells at stage 8-2.

(legend continued on next page)

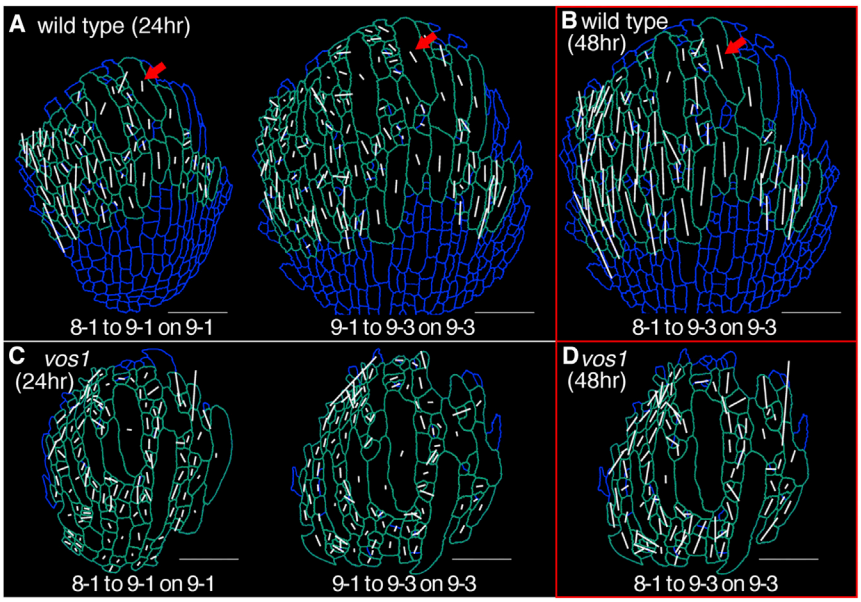

Figure 5. High Local Spatial Variability of Cellular Growth Promotes Organ Regularity

(A and C) The principal direction of growth in the maximal growth direction (PDG_{max}; white line) of the wild-type (A) and *vos1* (C) sepal cells calculated for each 24-hr interval show spatial and temporal variations (e.g., red arrows). Equivalent cells outlined in green are analyzed for wild-type and *vos1*. Only cells in which the growth is anisotropic are considered (maximum growth minus minimum growth >10%); PDG_{max} is not shown for cells growing isotropically where the direction is not well defined.

(B and D) PDG_{max} of wild-type cells calculated for the cumulative growth from 0 to 48 hrs (B) become much more coordinated across the sepal (e.g. red arrow), indicating that the plant is temporally averaging the variations seen at 24 hrs in (A). In contrast, the *vos1* sepal cells (D) show less temporal averaging of variability than wild-type, as the PDG_{max} for the cumulative 48-hrs growth are not aligned.

See also Figure S5.

Therefore, in the model we increased the correlation length of stiffness (the distance over which the stiffness is similar). We maintained temporal variation as in the spatiotemporal variability model. The simulated sepals from this "spatiotemporal variability model with low spatial variability" (ST-L) were less regular in shape than the simulated sepals produced by the ST model (Figures 2H–2K and Movie S5). They were also somewhat more variable in size than those produced by the initial spatiotemporal variability model (Figure 2J). Although the ST-L model increases size variability, it does not reproduce the extent of sepal size variation or the smaller average size of *vos1* sepals compared with wild-type. Thus, size and shape regularity can be partly uncoupled. An additional mechanism must contribute to sepal size variability in *vos1*, which we discuss below. To conclude, our revised model confirms that decreased local spatial variability can lead to irregularity of sepal shape. Thus, counterintuitively, we find that the higher level of local spatial variability found in wild-type sepals actually promotes sepal shape robustness.

Wild-Type Sepals Undergo Spatiotemporal Averaging of the Principal Direction of Growth, Resulting in Regularity, which Is Disrupted in *vos1* Mutants

To further explore how spatiotemporal averaging produces regular sepal shapes from variable cellular growth, we examined the principal directions of growth (PDGs) (Dumais and Kwiatkowska, 2002). Here we show only the vector in the direction maximal of growth, PDG_{max}. Cells growing isotropically (nearly equally in all directions) were excluded from analysis because in this case the PDGs become arbitrary. The PDG_{max} provide a visual indication of the coordination of growth directions between nearby cells and their overall alignment with the growth of the organ.

In wild-type sepals, the PDG_{max} of cells during short 24-hr growth intervals showed varied orientations (Figure 5A) in space and in time (Figure 5A, arrows), consistent with the spatial variability in cellular growth. We tested whether spatiotemporal variability averages to produce regular growth by examining PDGs calculated for longer time intervals. Over intervals of 48 hrs, we found that the PDG_{max} were highly aligned in the tip base axis of the sepal (Figure 5B, arrow), indicating that the spatial and temporal variability averages lead to regularity of plant growth.

In the *vos1* mutant sepal cells, the PDG_{max} were also spatially and temporally variable over 24-hr intervals; however, the PDG_{max} of *vos1* mutant cells calculated for the cumulative growth over 48 hrs were not well aligned with each other, indicating that *vos1* mutants are defective in the spatiotemporal averaging of growth direction (Figures 5C and 5D). Averaging was still defective over longer time intervals in *vos1* (Figure S5A). The reduced spatiotemporal averaging of variability in growth direction might explain the irregular shape of mutant sepals.

vos1 Is a Mutant of the FtsH4 Mitochondrial Protease

Genetic analysis and map-based cloning revealed that the *vos1* phenotype is caused by recessive mutations in the *FtsH4* gene (Figures 6A and S6A). Hence, we renamed the *vos1* mutant

(F) Graph plotting the average spatial variability in growth rate among neighboring cells ($<V_{area}>$ signifies the average of V_{area} over cells) for all the cells of each sepal at each floral stage imaged. Dotted black lines indicate the average spatial variability for all cells at all time points (WT 7.69%; *vos1* 5.32%). Note that *vos1* flowers tend to have decreased spatial variability (lower $<V_{area}>$; $p < 10^{-6}$, permutation test). The error bars represent the SE. Scale bar represents 50 μm.

(G and H) Local spatial variation in the cell-wall stiffness is decreased in *vos1* sepals. (G) Cell-wall stiffness of WT and *vos1* sepals at stage 10 measured by AFM is displayed as a heatmap with stiff points in red and soft points in blue. Cells are outlined in black based on topology maps. Each square represents one measurement point, which is 5 μm from the next measurement. (H) Graph plotting the average spatial variability in cell-wall stiffness ($<V_{AFM}>$) for WT and *vos1* sepals. Note that *vos1* sepals have decreased spatial variability in cell-wall stiffness (lower V_{AFM}) compared with WT. ***$p < 0.001$ (t test). n = 8 for WT and n = 9 for *vos1*. For the boxplots, the box extends from the lower to upper quartile values of the data, with a line at the median, and the whiskers extend past 1.5 of the interquartile range. See also Figure S4.

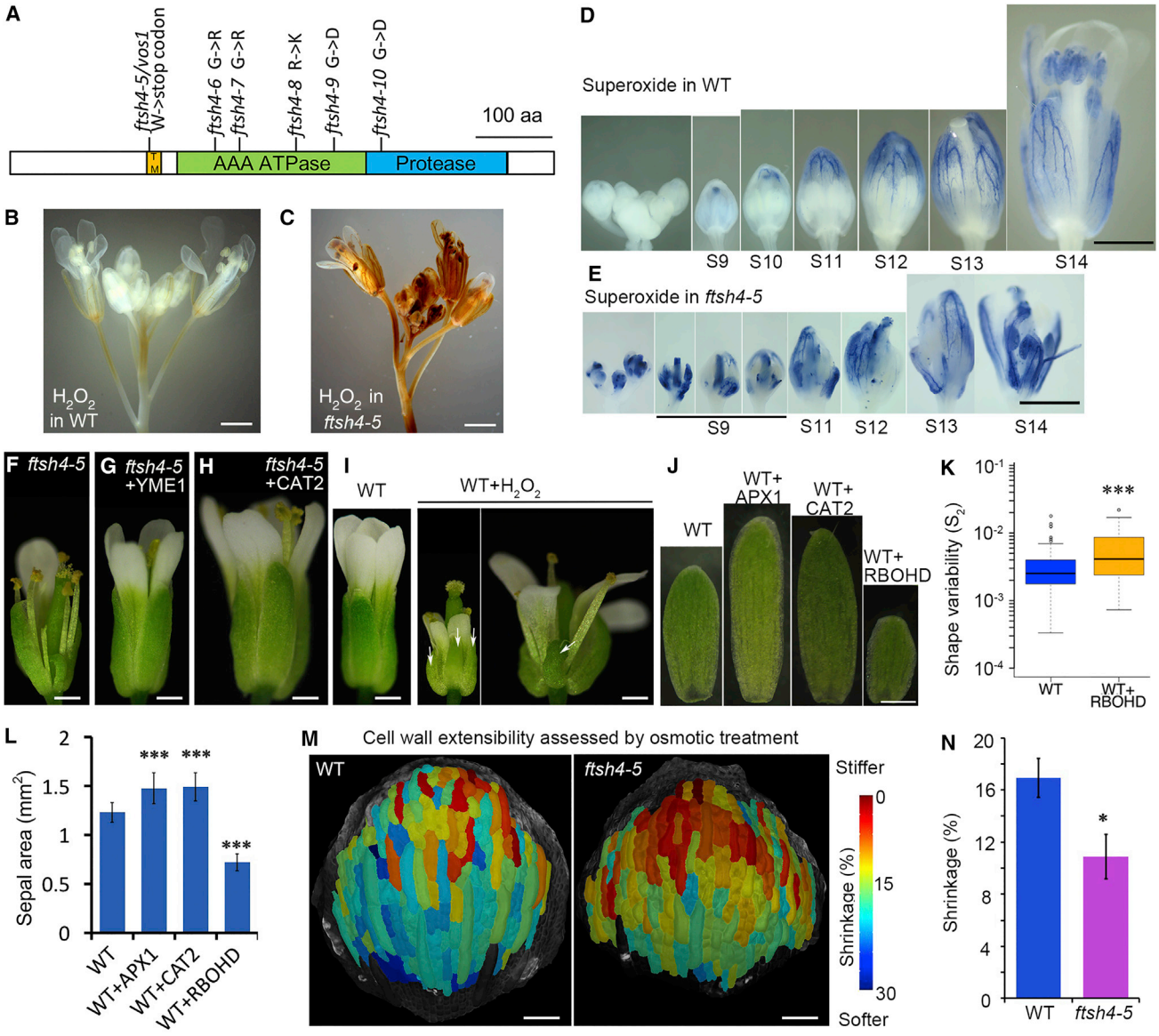

Figure 6. Reactive Oxygen Species Regulates Sepal Growth

(A) The protein domains of FtsH4 and the mutation sites of *ftsh4* alleles isolated in our study. The AAA-ATPase domain is shown in green, the protease domain in blue, and the transmembrane (TM) domain in orange.

(B and C) DAB staining for H_2O_2 in WT (B) and *ftsh4-5* (C) inflorescences. *ftsh4-5* mutants have a higher level of H_2O_2 throughout the inflorescences.

(D and E) NBT staining for superoxide in WT (D) and *ftsh4-5* (E) flowers. *ftsh4-5* has higher and more variable level of superoxide in the sepals. S9–S14: flowers at different stages.

(F and G) Expression of the yeast homolog gene of *FtsH4* (*YME1*) in *Arabidopsis ftsh4-5* mutants (F) rescues the variable sepal size phenotype (G).

(H) Overexpression of a catalase gene (*CAT2*), which catalyzes the decomposition of H_2O_2, in *ftsh4-5* rescues the irregular sepal size and shape phenotype.

(I) Wild-type (WT) flowers treated with 100 mM H_2O_2 (WT + H_2O_2) mimics *ftsh4* phenotype, generating sepals of variable sizes. The control WT was mock treated. Arrows show smaller sepals.

(J) WT flowers overexpressing a peroxidase gene (WT + APX1) or *CAT2* (WT + CAT2), which both decrease H_2O_2, have larger mature sepals. WT flowers overexpressing a NADPH oxidase gene (WT + RBOHD), which produce superoxide, have smaller mature sepals, as plotted in (L).

(K) WT + RBOHD flowers have larger variability in mature sepal (stage 14) shape S_2. WT data were reproduced from Figure 1D for comparison. ***$p < 0.001$, significant difference from WT (t test).

(L) Area of sepals in (J) confirming that decreasing ROS (WT + APX1 and WT + CAT2) increases sepal size while increasing ROS (WT + RBOHD) decreases sepal size. ***$p < 0.001$, significant difference from WT (t test). Data are mean ± SD. n = 68 for WT, n = 108 for WT + APX1, n = 145 for WT + CAT2, n = 69 for WT + RBOHD.

(legend continued on next page)

ftsh4-5; the *ftsh4-5* mutation causes a premature stop codon in the FtsH4 protein. *FtsH4* encodes an AAA-ATPase metalloprotease in the FtsH family (Janska et al., 2010; Sakamoto, 2003; Urantowka et al., 2005). FtsH proteases play key roles in quality control of membrane proteins in prokaryotic organisms and organelles of bacterial origin (i.e., mitochondria and chloroplasts) by eliminating abnormal membrane proteins and by promoting assembly of oxidative phosphorylation complexes (Ito and Akiyama, 2005). There are four FtsH proteases in *Arabidopsis* mitochondria: FtsH3, FtsH4, FtsH10, and FtsH11. Based on their topology in the membrane, FtsH4 and FtsH11 are classified as i-AAA proteases, which face the intermembrane space (Figure S6B), unlike matrix-facing m-AAA proteases FtsH3 and FtsH10 (Heazlewood et al., 2004; Sakamoto, 2003; Urantowka et al., 2005). Although phylogenetically related, FtsH4 and FtsH11 are functionally divergent, with their mutations affecting different aspects of plant growth (Gibala et al., 2009; Wagner et al., 2011; Zhang et al., 2014). They form independent homo-oligomeric i-AAA protease complexes in mitochondria, and FtsH11 is localized in both mitochondria and chloroplasts (Urantowka et al., 2005). FtsH4 is the only i-AAA protease required for the proper assembly and stability of oxidative phosphorylation complexes in *Arabidopsis* mitochondria (Kolodziejczak et al., 2007). Because the premature stop codon in *ftsh4-5* leads to the deletion of both the AAA-ATPase domain and the metalloprotease domain of FtsH4, *ftsh4-5* is likely to be a null mutant. Notably, from our screen, we isolated six *ftsh4* mutants. Although these had different mutations in *FtsH4*, all the alleles had variable sepal size phenotypes similar to that of *ftsh4-5* (Figures 6A and S6A).

FtsH4 homologs are highly conserved in *Escherichia coli*, yeast, humans, and *Arabidopsis* (Figure S6A). We rescued the variable sepal size phenotype of *ftsh4-5* mutants by transgenically expressing YME1, the yeast homolog of FtsH4; this demonstrated that the biochemical function of FtsH4 is conserved between eukaryotic kingdoms (Figures 6F and 6G).

The Increased Irregularity in *ftsh4* Sepals Is Caused by Increased ROS Levels

Building on the well-established role of FtsH4 homologs at the molecular and organelle levels, we focused our analysis on the cell and organ levels. Mutations in *FtsH4* have previously been shown to cause mitochondrial defects, including reduced cristae in mitochondria (Gibala et al., 2009). Mitochondrial defects can lead to increased levels of ROS (Pulliam et al., 2013). In addition, studies of chloroplast FtsH protease mutants have shown that high ROS accumulation is a major cause of morphological defects in leaves (Kato et al., 2009). Thus, we compared ROS levels between wild-type and mutant sepals. ROS include many molecules, with hydrogen peroxide (H_2O_2) and the superoxide radical (O_2^-) as the two major ones (Apel and Hirt, 2004). Using chemical stains specific for these two molecules, we found that *ftsh4-5* mutants have higher levels of both H_2O_2 and O_2^- in their sepals (Figures 6B–6E).

Remarkably, O_2^- formed a gradient in wild-type sepals that paralleled the wave of cellular maturation from the tip to the base of sepals (Figure 6D). High levels of O_2^- were first detectable in the sepal tip of flowers at stage 10, and progressed downward as the sepal grew, finally spreading to the whole sepal when it matured (stage 13; Figure 6D). In *ftsh4-5* sepals, O_2^- levels were higher and more variable. High levels of O_2^- were present in very young buds, and were unevenly distributed between different parts of a single sepal and between different sepals within the same flower (Figure 6E).

We next tested whether premature and uneven ROS were sufficient to disrupt sepal size uniformity. Wild-type flowers treated with H_2O_2 from early stages mimicked the *ftsh4* phenotype, generating variably sized sepals that were smaller on average (Figure 6I). We then decreased ROS levels in *ftsh4-5* by overexpressing *CATALASE 2* (*CAT2*). *CAT2* encodes a peroxide-metabolizing enzyme with high specificity for H_2O_2 (Mhamdi et al., 2010; Mittler et al., 2004). The transgene restored sepal size uniformity in the *ftsh4* mutant (Figures 6F and 6H), and transgenic flowers had lower ROS levels (Figure S6D). These results indicate that increased ROS levels cause the increased variability and decreased average size of *ftsh4* sepals.

ROS Act as a Growth Regulator in Wild-Type Sepals, Promoting Maturation and Termination of Growth

The pattern of O_2^- accumulation from the tip to the base of the wild-type sepal, coincident with the progressive maturation of the sepal from tip to base (Hervieux et al., 2016; Roeder et al., 2010), raised the question of whether O_2^- acts as an endogenous growth regulator controlling the termination of sepal growth. To test this, we decreased ROS levels in wild-type sepals by overexpressing either the catalase-encoding gene *CAT2* or the *ASCORBATE PEROXIDASE 1* (*APX1*) gene, which encodes another enzyme that scavenges H_2O_2 in *Arabidopsis* (Davletova et al., 2005; Ishikawa and Shigeoka, 2008; Mittler et al., 2004). Both kinds of transgenic plants had larger sepals than wild-type: 1.20 ± 0.13-fold for *APX1* (mean ± SD, n = 108) and 1.21 ± 0.12-fold for *CAT2* (mean ± SD, n = 145; Figures 6J and 6L). Overexpression of *CAT2* did not abolish the tip-to-base accumulation of O_2^-, but delayed it, consistently with the larger sepal sizes observed (Figure S6G). This demonstrated that decreasing the ROS level could promote sepal growth, and suggested that ROS act as endogenous signals to limit wild-type sepal growth. ROS may be general signals promoting a shift from cell division to maturation, as leaves had a similar pattern of O_2^- accumulation from tip to base correlating with the cessation of cell division, and overexpression of *CAT2* produced larger leaves (Figures S6C and S6E).

ftsh4 Sepals Exhibit Cellular Characteristics of Maturation Earlier than Wild-Type

To further test whether ROS act as maturation signals, we re-examined the growth of *ftsh4* flowers to determine whether their

(M and N) Cell walls are stiffer (had a lower percent shrinkage in osmotic treatments) in *ftsh4-5* sepals than in WT at stages 8–9. In the heatmap, the cells in red have low shrinkage and are stiffer than cells in blue with high shrinkage. (N) Plots of area shrinkage for the whole sepal. *$p < 0.1$, significant difference from WT (t test). Data are mean ± SD. n = 3 for WT and *ftsh4-5*.

For the boxplots, the box extends from the lower to upper quartile values of the data, with a line at the median, and the whiskers extend past 1.5 of the interquartile range. Scale bars represent 1 mm in (B)–(E), 500 μm in (F)–(J), and 50 μm in (M). See also Figures S6 and S7.

early increase in ROS correlated with early cellular maturation. Based on wild-type, we defined the region of maturing cells as those with slower growth rates and low cell division which we observed developing from tip to base (Figures 3C and S3E) (Hervieux et al., 2016; Roeder et al., 2010). Growth rates decreased in *ftsh4* mutants more quickly than in wild-type; growth rates of cells in mutant sepals at stage 9 appeared more similar to maturing cells of wild-type sepals at stage 12 (Figures 3D and 3G). The average of cellular growth rates over 12 hrs was lower in *ftsh4-5* (mean ± SD 1.28 ± 0.19, n = 472) than wild-type (mean ± SD 1.37 ± 0.22, n = 705) (Figure 3H). Accordingly, while wild-type cell lineages grew 3.43-fold larger on average in 48 hrs, *ftsh4* mutant cell lineages required 60 hrs to grow 3.3-fold (Figure 3H).

Maturation coincided with a shift from rapid cell division to slow cell division in wild-type sepals (Figures 3I and S3E). In *ftsh4* mutant sepals, the cell division rate remained low, throughout stages 7–11 (Figures 3I and S3E). Initially cell division and growth were balanced in wild-type sepals, yielding a constant average logarithm of cell area (Figures 3J and S3G). As cell division decreased, maturation coincided with a general increase in the average logarithm of cell area (Figure 3J). In *ftsh4* mutant sepals, the average logarithm of cell area began increasing at an unusually early stage of development (Figures 3J and S3H). Mature *ftsh4* sepals contained substantially fewer epidermal cells that were larger on average than wild-type sepal cells (Figures S3I and S3J), consistent with reduced cell division and early entry into cell expansion observed in the developing mutant sepals. In summary, *ftsh4* sepal cells behave like wild-type sepal cells of a later developmental stage, suggesting that *ftsh4* sepals begin maturation too early and that ROS promote cellular maturation in sepals.

ftsh4 Sepals Are Stiffer Than Wild-Type

One possible mechanism through which ROS may directly slow growth and reduce cellular growth variability is by modifying cell-wall mechanical properties (Barceló and Laura, 2009; Bell et al., 2009; Cosgrove, 2005; Lu et al., 2014). ROS may promote cell-wall stiffening by facilitating the formation of crosslinks between wall polysaccharides and glycoproteins (Fry, 2004; Ralph et al., 2004); alternatively, ROS may also loosen the cell wall by cleaving wall polysaccharides (Fry, 1998; Schopfer, 2001; Schweikert et al., 2000). As AFM allowed us to probe only small regions in the center of the sepal, we did not detect any difference in average stiffness between wild-type and *ftsh4* cell walls (Figure 4G). We therefore used osmotic treatments to assess the stiffness of the whole sepal (Kierzkowski et al., 2012). Wild-type sepals had a gradient with stiffer cells at the tip (Figures 6M and S5D), which matched the decreased growth rates of similarly staged sepal tips (compare with Figure 3C). Likewise, *ftsh4* flowers showed a gradient with stiffer cells at the tip; however, whole *ftsh4* sepals were stiffer than wild-type sepals (wild-type 17% ± 2.6% shrinkage; *ftsh4* 11% ± 1.7% shrinkage; mean ± SD, n = 3 sepals of each genotype; Figures 6M, 6N, and S5D). These results are consistent with a scenario in which ROS limit growth in sepals by increasing the number of crosslinks in cell walls.

Reduced Cellular Variability and Spatiotemporal Averaging Correlate with ROS Accumulation in Maturing Wild-Type Sepal Tips

If ROS signals in wild-type sepals promote maturation, and the *ftsh4* phenotype is generated by an overabundance of ROS signal (essentially a gain of function), then we would expect to observe inhibition of spatiotemporal averaging of growth in the tips of wild-type sepals as the ROS signal initiates there. As expected, the maturing tips of wild-type sepals exhibited reduced local spatial variability in growth (Figure S4D) and reduced spatiotemporal averaging of PDGs (Figures S5B and S5C) but no change in temporal variability of growth (Figures S4A and S4B), compared with the middle of the sepal, where ROS had not yet accumulated. These results are consistent with ROS inhibiting cellular variability and spatiotemporal averaging during wild-type sepal maturation.

Spatiotemporal Averaging Combined with a Maturation Gradient Regulated by ROS Produce Sepal Regularity

Based on our observation that O_2^- accumulates and growth slows from the sepal tip downward (Figures 3C and 6D), we postulated that ROS act as signals that terminate sepal growth. Therefore, we created an "arrest front" (AF) model, in which we initiate a ROS signal at the tip when the sepal reaches a defined height, with variability in the initiation height (see Experimental Procedures). The signal propagates down the developing sepal and growth stops when the signal reaches the base (Figure 7A). This AF model was initially implemented in the NV model template to examine the effects of variability in arrest front alone. AF models with low variability in the initiation height produce robust sepal sizes (e.g., arrest front height 3 ± 0.05 SD in Figure 7B), whereas large variability in the arrest front initiation height produced large variation in sepal size (e.g., 2.7 ± 0.5 SD in Figure 7B).

However, sepals produced by the AF model did not show any variation in shape. Therefore, to model wild-type sepals, we combined the AF model (ROS arrest front initiation height = 3.0 ± 0.04 SD) with the ST model, which produced robust sepals with little variation in shape (S_2) and size (coefficient of variation, CV), comparable with wild-type sepals (Figures 7C, 7E, and 7G–7H compared with Figures 1C, 1E, and 1F; Movie S6). To fit simulation output to experiments, we chose a level of temporal variability corresponding to a renewal value of 10%, meaning that 10% of the mechanical properties are updated from one computational step to the next (Figures S2F and S2G).

To model *ftsh4* sepals, we combined the AF model initiated with a lower and more variable arrest front reflecting the early and variable accumulation of O_2^- (Figure 6E; ROS arrest front initiation height = 2.7 ± 0.15 SD) with a reduced spatiotemporal variability model (ST-L correlation length of 1/3.5). This model reproduced both the size (CV) and shape (S_2) variability of *ftsh4* sepals relative to wild-type (Figures 7D–7F compared with Figures 1C–1F; Movie S6). Thus, modeling and experiments together suggest that the size irregularity of *ftsh4* sepals arises primarily from the variable accumulation of ROS, whereas the shape irregularity of *ftsh4* sepal arises from the decreased cellular spatial variability and reduced spatiotemporal averaging.

To test this conclusion experimentally, we induced more uniform ROS accumulation in real sepals. Induction of ectopic

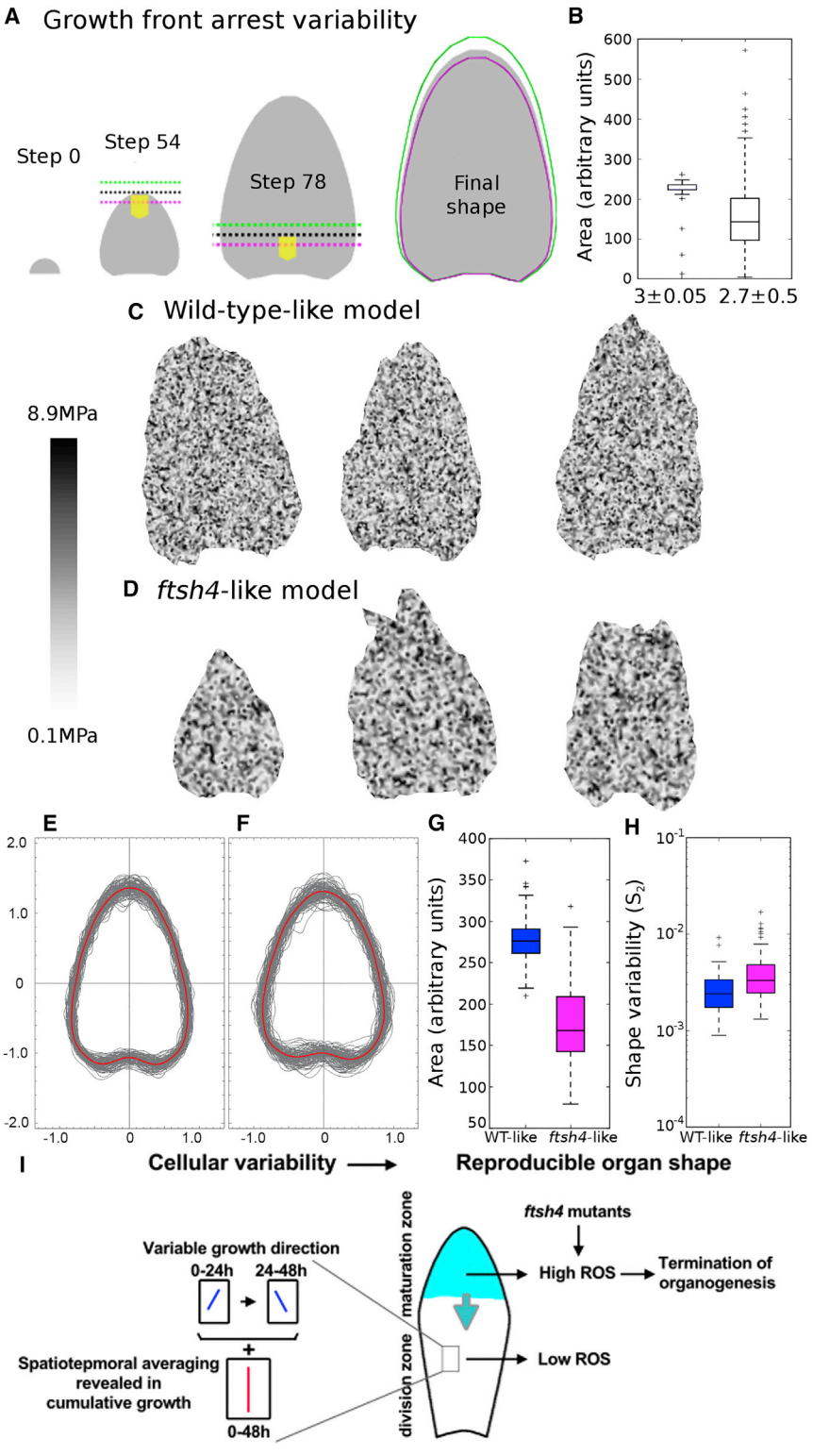

Figure 7. Reproducible Organs Arise from Variable Cells

(A and B) Examples of simulation steps of the arrest front model of sepal growth. When the sepal reaches a threshold in length, a front (dotted black line) propagates at constant velocity toward the base, arresting growth when the front reaches the base, which determines the final sepal size and shape. If the height of the threshold is variable, then sepal size is also variable (green high threshold, larger size; magenta low threshold, smaller size). This model was run with uniform stiffness based on the NV model from Figure 2A to isolate the effect of the arrest front.

(B) Boxplot of simulated sepal area (a.u., initial area ~1) with two sets of parameters: arrest front with a little noise on threshold (3.0 ± 0.05), and arrest front with smaller average threshold and enhanced noise on threshold (2.7 ± 0.5) (arrest front follows a Gaussian curve of parameters mean ± SD).

(C–H) The wild-type and *vos1* phenotypes have been reproduced with the model. (C) Three replicates of the wild-type-like model, with parameters: correlation length 1/5, renewal 1/10 (see Figure S2), arrest front threshold 3.0 ± 0.08. (D) Three replicates of the *vos1*-like model, with parameters: correlation length 1/3.5, renewal 1/10, front arrest 2.7 ± 0.15. (E) Normalized simulated sepal outlines showing shape variability of the wild-type-like model. (F) Normalized simulated sepal outlines showing increased shape variability of the *ftsh4*-like model. (G) Simulated sepal area of the wild-type-like model (WT-like) and the *ftsh4*-like model (*vos1*). Note that the simulated *ftsh4*-like sepal has a smaller median size and larger range than the wild-type-like sepal and is comparable with the real sepal data in Figure 1C (mean ratio of area mutant/wild-type: experimental data = 0.69, model = 0.62; coefficient of variation of wild-type: experimental data = 0.08, model = 0.10; coefficient of variation of mutant: experimental data = 0.32, model = 0.28) (f test, $p < 10^{-6}$).

(H) Simulated sepal shape variability of the wild-type-like model (WT-like) and the *ftsh4*-like model (t test, $p < 10^{-5}$). Note that the simulated *ftsh4*-like sepal has increased shape variability comparable with the real sepal data in Figure 1F (shape variation S_2 for WT sepals: experimental data = 0.00253, model = 0.00242; shape variation S_2 for mutant sepals: experimental data = 0.00423, model = 0.00331). The statistics in (B, G–H) were obtained over 100 replicates (simulation runs).

(I) Conceptual summary. Spatiotemporal averaging of cellular growth variability produces regular organ shapes. For instance, the maximum principal direction of growth (PDG_{max}; blue line) in a cell may tilt to the left and then later to the right such that the variability averages so that the cumulative growth (red PDG) is highly regular, aligning with other cells, to produce uniform organs. Our data suggest that ROS (aqua) inhibit spatiotemporal averaging while promoting the maturation of cells, reduction of cell division, and termination of growth. ROS accumulate in maturing cells starting at the tip and descending toward the base of the sepal (aqua arrow). Increased, variable, and premature accumulation of ROS in *ftsh4* mutants causes irregular sepal shapes by reducing cellular variability and inhibiting spatiotemporal averaging and irregular sepal sizes by variable initiation of the arrest front.

For the boxplots, the box extends from the lower to upper quartile values of the data, with a line at the median, and the whiskers extend past 1.5 of the interquartile range. See also Movies S1, S4, and S6.

expression of an NADPH oxidase, which produces O_2^-, caused the sepals to be uniformly smaller, with variability in sepal size comparable with wild-type sepals (mean ± SD 0.69 ± 0.10 mm^2, n = 69; Figures 6J and 6L; compared with wild-type 1.23 ± 0.10 mm^2), but sepals were irregular in shape with variability in shape similar to that of *ftsh4* mutants (NADPH oxidase S_2 = 0.0041 ± 0.0005, n = 69; *ftsh4* S_2 = 0.0042 ± 0.0004, n = 518; wild-type S_2 = 0.0025 ± 0.0001, n = 215; mean ± SE; Figures 1F, 6K, and S6E). This result confirms that the variability of ROS accumulation in *ftsh4* mutants contributes to the irregular sizes, and is consistent with ROS accumulation reducing cellular growth variability and inhibiting spatiotemporal averaging.

DISCUSSION

We address the key question of how organs can reach precise shapes and sizes despite the variable growth of their cells. We found that organs average variations in cellular growth over space and time to achieve constant morphology. First, using computational simulation, we predicted that robust shapes could emerge from a combination of spatial and temporal variability in a phenomenon termed spatiotemporal averaging. This phenomenon was observed in the cellular growth of wild-type sepals. For example, if a cell's growth is oriented toward the left at one time point and then toward the right at another time point, the total growth averages to vertical, and aligns with neighboring cells (Figure 7I). In this way, organs can maintain robust morphology.

We verified this model by screening for mutants in *Arabidopsis* with disrupted organ uniformity (i.e., mutants with differently sized and shaped sepals in the same plant). We identified *ftsh4*, which disrupted regularity in floral organ size and shapes, due to premature and uneven ROS accumulation. First, ROS accumulation inhibited spatiotemporal averaging in *ftsh4* mutants, which caused irregularity primarily in shape. In *ftsh4* mutants the local spatial variability in cell growth decreased. Similarly, model simulations with decreased local spatial variability produced more irregular sepal shapes. Imagine a cell that starts growing awry, e.g., in the "wrong" direction. If local spatial variability is high, its neighbors will not follow it and will somehow compensate for the "wrong" direction. If local spatial variability is low, its neighbors are correlated with this cell and will also grow awry, which can affect overall organ growth. Second, the uneven ROS accumulation in *ftsh4* mutants caused substantial variability in sepal size. Cellular growth in *ftsh4* mutants exhibited many characteristics of sepal cells maturing earlier than in wild-type, suggesting that ROS act as growth regulators promoting maturation (Figure 7I). Enzymatically reducing ROS in *ftsh4* mutants restored uniform sepal size and shape, which demonstrated that the abnormal ROS accumulation caused the failure of organ size uniformity in *ftsh4* mutants.

ROS also accumulated in the maturing cells of wild-type sepals, coincident with a wave of arrest propagating from tip to base (Figure 7I). Interestingly, ROS accumulation in wild-type sepal tips also inhibited spatiotemporal averaging, but since these cells were already slowing their growth and maturing, this had little effect on sepal regularity. We demonstrated that ROS regulates wild-type sepal growth by reducing ROS enzymatically in wild-type sepals, which caused the sepals to grow significantly larger than wild-type. Thus, ROS is a key growth regulator that promotes maturation and termination of organ growth while simultaneously inhibiting spatiotemporal averaging. The correct pattern and timing of ROS accumulation in the sepal is required to maintain organ regularity.

Spatiotemporal Averaging as a General Mechanism to Deal with Stochasticity

Growth on the cellular level is highly variable. In plants, such variability is also found for cell-wall stiffness measured with AFM (Milani et al., 2011; Yakubov et al., 2016), consistent with our results on sepals. In addition, experiments and modeling have shown that feedback loops between mechanical stress and plant cell growth orientation can promote heterogeneity in the growth rates and orientations between neighboring cells in *Arabidopsis* (Uyttewaal et al., 2012).

In theory, time integration (temporal filtering) can explain the maintenance of robustness in the face of variability originating from random or unpredictable cellular or molecular behaviors (Lander, 2011). In a developmental context, spatiotemporal averaging has been proposed to account for precise distributions of *hunchback* mRNA in the *Drosophila* embryo despite stochastic *hunchback* transcription (Little et al., 2013). The use of spatiotemporal averaging to overcome noise in biology at these two different scales (transcript to cell and cell to organ) suggests that it may be a common mechanism ensuring robustness in many biological processes.

Variability on the cellular level could be beneficial to organisms. Unicellular organisms use expression variability to create population heterogeneity, to switch between different physiological states, and to deal with environmental stresses (Blake et al., 2006; Kussell and Leibler, 2005). Expression variability has been proposed to facilitate the evolution of gene regulation (Wolf et al., 2015). Maintenance of growth heterogeneity within the shoot apical meristem has also been proposed to prime cells for differential growth and organogenesis (Uyttewaal et al., 2012). Our results indicate that cellular variability yields consistent organs as the reduced local spatial variability in cellular growth in area of *ftsh4* mutants leads to the production of more variable organs.

The observation that spatiotemporal averaging is decreased in the wild-type sepal tip as ROS accumulate to promote maturation and terminate organ growth suggests that there might be an inherent conflict between terminating organ growth and maintaining regularity through spatiotemporal averaging. In wild-type, this inhibition of spatiotemporal averaging occurs only during maturation when growth slows, so it does not create highly variable shapes as seen in the *ftsh4* mutant, where spatiotemporal averaging is blocked throughout much of sepal development. It may, however, account for the small amount of shape variability in wild-type.

ROS as a Signal that Promotes Cellular Maturation and Growth Arrest

Previous screens for mutations in genes regulating robustness have been done only in yeast (Bauer et al., 2015; Boukhibar and Barkoulas, 2015; Levy and Siegal, 2008; Rinott et al., 2011). These yeast studies show that genes that are master regulators of robustness (also called phenotypic capacitors) encode

proteins that are often part of highly connected nodes in the gene regulatory networks. In both plants and animals, ROS form highly connected nodes bridging several signal transduction networks that regulate growth and cell proliferation (Covarrubias et al., 2008; Mittler et al., 2011; Xia et al., 2015).

In addition to the well-established role of ROS in plant stress responses (Choudhury et al., 2013; Perez and Brown, 2014), our work and that of others show that ROS signaling is important for plant development (Foreman et al., 2003; Gapper, 2006; Rodríguez et al., 2002). Previous studies have suggested that ROS could affect organ growth through controlling cell division in many organisms (Boonstra and Post, 2004). In mammalian cells and *Drosophila* eye imaginal disks, increasing ROS induces the CDK inhibitors that induce cell-cycle arrest or delay (Owusu-Ansah et al., 2008; Russo et al., 1995). As well as limiting cell proliferation, ROS can also affect cell enlargement. In *Arabidopsis* roots, different types of ROS modulate the balance between cell proliferation and cell elongation creating the characteristic zones of the root meristem, which affect root growth (Reyt et al., 2015; Tsukagoshi et al., 2010). In leaves, reducing ROS levels due to elevated level of antioxidants will delay cell proliferation exit, thus resulting in more cells (Xue et al., 2015). On the other hand, modulating ROS balance in leaves by increasing peroxidase activity will also lead to smaller cells (Lu et al., 2014). Moreover, our dynamic analysis of cell and organ growth reveals that ROS play an important role in organ size and shape robustness through limiting cell division and promoting maturation, as well as through inhibiting spatiotemporal averaging of cellular growth variability.

In yeast, mutating the yeast FtsH4 homolog YME1 results in growth defects (Thorsness and Fox, 1993; Thorsness et al., 1993). Expressing yeast YME1 in *Arabidopsis* rescues the *ftsh4* mutant, suggesting conserved biochemical function across eukaryotes. Our analyses of yeast *yme1* mutants revealed that, under some growth conditions, *yme1* mutants produced higher levels of ROS and had lower proliferation than wild-type (Figure S7). These results are consistent with previous studies indicating a role for ROS in inhibiting cell proliferation.

In addition to its signaling role, our osmotic treatments support a role for ROS in directly arresting growth mechanically by stiffening cell walls through the formation of crosslinks between wall polysaccharides and glycoproteins (Barceló and Laura, 2009; Bell et al., 2009; Cosgrove, 2005; Fry, 2004; Lu et al., 2014; Ralph et al., 2004). As cell-wall stiffness controls growth rate, this could explain the reduced spatial variability in the growth rate of the *ftsh4* mutant (Figures 4G and 4H).

To conclude, the abnormal accumulation of ROS in *ftsh4* mutants disrupts sepal uniformity in two ways. First, it creates a more variable termination signal, causing the sepal to mature early. Second, it inhibits spatiotemporal averaging of cellular variability, resulting in oddly shaped sepals.

EXPERIMENTAL PROCEDURES

Detailed methods are described in Supplemental Experimental Procedures.

Plant Material and Treatment

Arabidopsis accession *Col*-0 plants are used as wild-type throughout. Mutants were generated by ethyl methanesulfonate mutagenesis. Mutations were isolated using standard map-based cloning (Lukowitz et al., 2000). Allelism tests were conducted between different *ftsh4* alleles. Plants were examined under a dissecting microscope for the sepal phenotype. Flowers were staged according to Smyth et al. (1990).

The *YME1* gene, *CAT2* gene, and *APX1* gene full-length cDNA were amplified and LR recombined into the gateway vector pB7WG2. Full-length cDNA of the *RBOHD* gene was used for dexamethasone-inducible expression from the pOp/LhGR expression system (Craft et al., 2005). All of the intermediate and final plasmids used for plant transformation were verified by sequencing. The final constructs were individually transformed into *ftsh4-5* or wild-type plants by *Agrobacterium*-mediated floral dipping.

For H_2O_2 treatment or dexamethasone induction, flowers were dipped into 100 mM H_2O_2 or 5 μM dexamethasone solution once a day for 7 days.

Microscopy and Image Analysis

Low-magnification whole sepal/flower images were photographed using a dissecting microscope mounted with a camera.

For sepal area and shape measurements, custom Python programs (Data S1) were used to extract the contour and measure the area of each stage 14 sepal. The data were sorted, analyzed, and plotted in Microsoft Excel or the statistical software R. The shape variability was studied by analyzing the sepal's contour points using Fourier decomposition. The contours were normalized with respect to the average radius. The squared deviation of a given contour from the median contour was used to quantify shape variability.

AFM was performed on off-plant stage 10 flowers, using a JPK Nanowizard III atomic force microscope with an extended vertical range of 100 μm. The cantilevers (SCANASYST-AIR, Bruker) had a nominal spring constant of 7 N/m and a pyramid-shaped tip (tip angle 18°, nominal radius 2 nm). Scanning electron microscopy was performed using a Leica 440 (Roeder et al., 2010).

For live imaging, flowers expressing pAR169 (*pATML1::RCI2A-mCitrine*) were imaged with a Zeiss LSM710 confocal microscope every 12 hrs. MorphoGraphX was used to segment individual cells, track cell lineages, and calculate cell area and PDGs. The spatial and temporal variability in the growth of cell area used the consecutive areas of the cells with the same lineage, based on the area calculated in MorphoGraphX.

Sepal stiffness was measured by treating stage 8–9 sepals with 0.4 M NaCl solution for 30 min, imaging the cell wall with a Leica SP8 confocal microscope, and calculating the cell shrinkage in MorphoGraphX.

In situ detection of H_2O_2 and O_2^- was carried out by 3,3′-diaminobenzidine and nitroblue tetrazolium staining, respectively.

Computational Modeling

A continuous mechanical model for sepal morphogenesis was built, based on a model previously developed for fission yeast (Bonazzi et al., 2014). Only surface cell walls were modeled, yielding a two-dimensional material with a prescribed distribution of elastic modulus, E. Morphogenesis occurred by successive increments in area. The model was implemented in Freefem++ (Hecht, 2012) and the results were analyzed using Python scripts (Data S1).

SUPPLEMENTAL INFORMATION

Supplemental Information includes Supplemental Experimental Procedures, seven figures, six movies, and one data file and can be found with this article online at http://dx.doi.org/10.1016/j.devcel.2016.06.016.

AUTHOR CONTRIBUTIONS

Conception and design of experiments: L.H., A.H.K.R., A.B., O.H., C.B.L., T.K., and R.S.S. Isolation and characterization of *ftsh4* mutant: L.H., C.C., and A.H.K.R. Software for extraction of sepal contours: A.K. Variability of organ size analysis: L.H., M.Z., and C.C. Variability of organ shape analysis: C.B.L. Computational model development: M.D. and A.B.. AFM: M.D. and A.B. Live imaging and analysis: L.H. MorphoGraphX development for this project: A.S., A.-L.R.-K., and R.S.S. Computational analysis of the variability of growth: S.T., C.B.L., and T.K. ROS experiments: L.H. and Y.Z. Osmotic treatments: A.S. and R.S.S. Writing of the manuscript: L.H. and A.H.K.R. Revising and editing of the manuscript: L.H., M.D., S.T., A.-L.R.-K., Y.Z., C.C., R.S.S., T.K., O.H., C.B.L., A.B., and A.H.K.R.

ACKNOWLEDGMENTS

We thank Nathan Hervieux, Heather Meyer, Dana Robinson, Phoebe Roeder, Michael Scanlon, and Erich Schwarz for comments on the manuscript. We thank Li Xu and Anthony Bretscher for yeast reagents. We thank Chelsea Alvarado and Madhurima Chowdhury for technical assistance. This work was supported by Human Frontier Science Program grant RGP0008/2013 (A.B./O.H., A.H.K.R., C.B.L., R.S.S.).

Received: November 24, 2015
Revised: May 4, 2016
Accepted: June 9, 2016
Published: July 11, 2016

REFERENCES

Anastasiou, E., Kenz, S., Gerstung, M., MacLean, D., Timmer, J., Fleck, C., and Lenhard, M. (2007). Control of plant organ size by *KLUH*/*CYP78A5*-dependent intercellular signaling. Dev. Cell *13*, 843–856.

Andriankaja, M., Dhondt, S., De Bodt, S., Vanhaeren, H., Coppens, F., De Milde, L., Mühlenbock, P., Skirycz, A., Gonzalez, N., Beemster, G.T.S., et al. (2012). Exit from proliferation during leaf development in *Arabidopsis thaliana*: a not-so-gradual process. Dev. Cell *22*, 64–78.

Apel, K., and Hirt, H. (2004). Reactive oxygen species: metabolism, oxidative stress, and signal transduction. Annu. Rev. Plant Biol. *55*, 373–399.

Armour, W.J., Barton, D.A., Law, A., and Overall, R.L. (2015). Differential growth in periclinal and anticlinal walls during lobe formation in *Arabidopsis* cotyledon pavement cells. Plant Cell *27*, 2484–2500.

Barbier de Reuille, P., Routier-Kierzkowska, A.L., Kierzkowski, D., Bassel, G.W., Schüpbach, T., Tauriello, G., Bajpai, N., Strauss, S., Weber, A., Kiss, A., et al. (2015). MorphoGraphX: a platform for quantifying morphogenesis in 4D. eLife *4*, e05864.

Barceló, A.R., and Laura, V.G.R. (2009). Reactive oxygen species in plant cell walls. In Reactive Oxygen Species in Plant Signaling, L.A. del Rio and A. Puppo, eds. (Springer), pp. 73–93.

Bassel, G.W., Stamm, P., Mosca, G., Barbier de Reuille, P., Gibbs, D.J., Winter, R., Janka, A., Holdsworth, M.J., and Smith, R.S. (2014). Mechanical constraints imposed by 3D cellular geometry and arrangement modulate growth patterns in the *Arabidopsis* embryo. Proc. Natl. Acad. Sci. USA *111*, 8685–8690.

Bauer, C.R., Li, S., and Siegal, M.L. (2015). Essential gene disruptions reveal complex relationships between phenotypic robustness, pleiotropy, and fitness. Mol. Syst. Biol. *11*, 773.

Bell, E., Takeda, S., and Dolan, L. (2009). Reactive oxygen species in growth and development. In Reactive Oxygen Species in Plant Signaling, L.A. del Rio and A. Puppo, eds. (Berlin, Heidelberg: Springer), pp. 43–53.

Blake, W.J., Balázsi, G., Kohanski, M.A., Isaacs, F.J., Murphy, K.F., Kuang, Y., Cantor, C.R., Walt, D.R., and Collins, J.J. (2006). Phenotypic consequences of promoter-mediated transcriptional noise. Mol. Cell *24*, 853–865.

Bonazzi, D., Julien, J.-D., Romao, M., Seddiki, R., Piel, M., Boudaoud, A., and Minc, N. (2014). Symmetry breaking in spore germination relies on an interplay between polar cap stability and spore wall mechanics. Dev. Cell *28*, 534–546.

Boonstra, J., and Post, J.A. (2004). Molecular events associated with reactive oxygen species and cell cycle progression in mammalian cells. Gene *337*, 1–13.

Boudon, F., Chopard, J., Ali, O., Gilles, B., Hamant, O., Boudaoud, A., Traas, J., and Godin, C. (2015). A computational framework for 3D mechanical modeling of plant morphogenesis with cellular resolution. PLoS Comput. Biol. *11*, e1003950.

Boukhibar, L.M., and Barkoulas, M. (2015). The developmental genetics of biological robustness. Ann. Bot. *117*, 699–707.

Chebli, Y., Kaneda, M., Zerzour, R., and Geitmann, A. (2012). The cell wall of the *Arabidopsis* pollen tube—spatial distribution, recycling, and network formation of polysaccharides. Plant Phys. *160*, 1940–1955.

Choudhury, S., Panda, P., Sahoo, L., and Panda, S.K. (2013). Reactive oxygen species signaling in plants under abiotic stress. Plant Signal. Behav. *8*, e23681.

Coen, E.S., Rolland-Lagan, A.-G., Matthews, M., Bangham, J.A., and Prusinkiewicz, P. (2004). The genetics of geometry. Proc. Natl. Acad. Sci. USA *101*, 4728–4735.

Colombani, J., Andersen, D.S., and Léopold, P. (2012). Secreted peptide Dilp8 coordinates *Drosophila* tissue growth with developmental timing. Science *336*, 582–585.

Cosgrove, D.J. (1993). Wall extensibility: its nature, measurement and relationship to plant cell growth. New Phytol. *124*, 1–23.

Cosgrove, D.J. (2005). Growth of the plant cell wall. Nat. Rev. Mol. Cell Biol. *6*, 850–861.

Covarrubias, L., Hernández-García, D., Schnabel, D., Salas-Vidal, E., and Castro-Obregón, S. (2008). Function of reactive oxygen species during animal development: passive or active? Dev. Biol. *320*, 1–11.

Craft, J., Samalova, M., Baroux, C., Townley, H., Martinez, A., Jepson, I., Tsiantis, M., and Moore, I. (2005). New pOp/LhG4 vectors for stringent glucocorticoid-dependent transgene expression in *Arabidopsis*. Plant J. *41*, 899–918.

Cui, M.-L., Copsey, L., Green, A.A., Bangham, J.A., and Coen, E.S. (2010). Quantitative control of organ shape by combinatorial gene activity. PLoS Biol. *8*, e1000538.

Cunha, A., Tarr, P.T., Roeder, A.H.K., Altinok, A., Mjolsness, E., and Meyerowitz, E.M. (2012). Computational analysis of live cell images of the *Arabidopsis thaliana* plant. Methods Cell Biol. *110*, 285–323.

Davletova, S., Rizhsky, L., Liang, H., Shengqiang, Z., Oliver, D.J., Coutu, J., Shulaev, V., Schlauch, K., and Mittler, R. (2005). Cytosolic ascorbate peroxidase 1 is a central component of the reactive oxygen gene network of *Arabidopsis*. Plant Cell *17*, 268–281.

Day, S.J., and Lawrence, P.A. (2000). Measuring dimensions: the regulation of size and shape. Development *127*, 2977–2987.

De Veylder, L., Beeckman, T., Beemster, G.T., Krols, L., Terras, F., Landrieu, I., van der Schueren, E., Maes, S., Naudts, M., and Inzé, D. (2001). Functional analysis of cyclin-dependent kinase inhibitors of *Arabidopsis*. Plant Cell *13*, 1653–1668.

Deprost, D., Yao, L., Sormani, R., Moreau, M., Leterreux, G., Nicolaï, M., Bedu, M., Robaglia, C., and Meyer, C. (2007). The *Arabidopsis* TOR kinase links plant growth, yield, stress resistance and mRNA translation. EMBO Rep. *8*, 864–870.

Dinneny, J.R., Yadegari, R., Fischer, R.L., Yanofsky, M.F., and Weigel, D. (2004). The role of *JAGGED* in shaping lateral organs. Development *131*, 1101–1110.

Disch, S., Anastasiou, E., Sharma, V.K., Laux, T., Fletcher, J.C., and Lenhard, M. (2006). The E3 ubiquitin ligase BIG BROTHER controls *Arabidopsis* organ size in a dosage-dependent manner. Curr. Biol. *16*, 272–279.

Doupé, D.P., Klein, A.M., Simons, B.D., and Jones, P.H. (2010). The ordered architecture of murine ear epidermis is maintained by progenitor cells with random fate. Dev. Cell *18*, 317–323.

Dumais, J., and Kwiatkowska, D. (2002). Analysis of surface growth in shoot apices. Plant J. *31*, 229–241.

Elsner, J., Michalski, M., and Kwiatkowska, D. (2012). Spatiotemporal variation of leaf epidermal cell growth: a quantitative analysis of *Arabidopsis thaliana* wild-type and triple *cyclinD3* mutant plants. Ann. Bot. *109*, 897–910.

Ferjani, A., Horiguchi, G., Yano, S., and Tsukaya, H. (2007). Analysis of leaf development in *fugu* mutants of *Arabidopsis* reveals three compensation modes that modulate cell expansion in determinate organs. Plant Phys. *144*, 988–999.

Foreman, J., Demidchik, V., Bothwell, J., and Mylona, P. (2003). Reactive oxygen species produced by NADPH oxidase regulate plant cell growth. Nature *422*, 442–446.

Fry, S.C. (1998). Oxidative scission of plant cell wall polysaccharides by ascorbate-induced hydroxyl radicals. Biochem. J. *332*, 507–515.

Fry, S.C. (2004). Oxidative coupling of tyrosine and ferulic acid residues: intra- and extra-protoplasmic occurrence, predominance of trimers and larger products, and possible role in inter-polymeric cross-linking. Phytochem. Rev. *3*, 97–111.

Gapper, C. (2006). Control of plant development by reactive oxygen species. Plant Phys. *141*, 341–345.

Garelli, A., Gontijo, A.M., Miguela, V., Caparros, E., and Dominguez, M. (2012). Imaginal discs secrete insulin-like peptide 8 to mediate plasticity of growth and maturation. Science *336*, 579–582.

Gibala, M., Kicia, M., Sakamoto, W., Gola, E.M., Kubrakiewicz, J., Smakowska, E., and Janska, H. (2009). The lack of mitochondrial AtFtsH4 protease alters *Arabidopsis* leaf morphology at the late stage of rosette development under short-day photoperiod. Plant J. *59*, 685–699.

Green, A.A., Kennaway, J.R., Hanna, A.I., Bangham, J.A., and Coen, E.S. (2010). Genetic control of organ shape and tissue polarity. PLoS Biol. *8*, e1000537.

Gupta, P.B., Fillmore, C.M., Jiang, G., Shapira, S.D., Tao, K., Kuperwasser, C., and Lander, E.S. (2011). Stochastic state transitions give rise to phenotypic equilibrium in populations of cancer cells. Cell *146*, 633–644.

Heazlewood, J.L., Tonti-Filippini, J.S., Gout, A.M., Day, D.A., Whelan, J., and Millar, A.H. (2004). Experimental analysis of the *Arabidopsis* mitochondrial proteome highlights signaling and regulatory components, provides assessment of targeting prediction programs, and indicates plant-specific mitochondrial proteins. Plant Cell *16*, 241–256.

Hecht, F. (2012). New development in FreeFem++. J. Numer. Math. *20*, 251–266.

Hemerly, A., Engler, J. de A., Bergounioux, C., Van Montagu, M., Engler, G., Inzé, D., and Ferreira, P. (1995). Dominant negative mutants of the Cdc2 kinase uncouple cell division from iterative plant development. EMBO J. *14*, 3925–3936.

Hervieux, N., Dumond, M., Sapala, A., Routier-Kierzkowska, A.-L., Kierzkowski, D., Roeder, A.H.K., Smith, R.S., Boudaoud, A., and Hamant, O. (2016). A mechanical feedback restricts sepal growth and shape in *Arabidopsis*. Curr. Biol. *26*, 1019–1028.

Horiguchi, G., and Tsukaya, H. (2011). Organ size regulation in plants: insights from compensation. Front. Plant Sci. *2*, 24.

Horiguchi, G., Kim, G.-T., and Tsukaya, H. (2005). The transcription factor AtGRF5 and the transcription coactivator AN3 regulate cell proliferation in leaf primordia of *Arabidopsis thaliana*. Plant J. *43*, 68–78.

Ishikawa, T., and Shigeoka, S. (2008). Recent advances in ascorbate biosynthesis and the physiological significance of ascorbate peroxidase in photosynthesizing organisms. Biosci. Biotech. Biochem. *72*, 1143–1154.

Ito, K., and Akiyama, Y. (2005). Cellular functions, mechanism of action, and regulation of FtsH protease. Annu. Rev. Microbiol. *59*, 211–231.

Janska, H., Piechota, J., and Kwasniak, M. (2010). ATP-dependent proteases in biogenesis and maintenance of plant mitochondria. Biochim. Biophys. Acta *1797*, 1071–1075.

Karidas, P., Challa, K.R., and Nath, U. (2015). The *tarani* mutation alters surface curvature in *Arabidopsis* leaves by perturbing the patterns of surface expansion and cell division. J. Exp. Bot. *66*, 2107–2122.

Kato, Y., Miura, E., Ido, K., Ifuku, K., and Sakamoto, W. (2009). The variegated mutants lacking chloroplastic FtsHs are defective in D1 degradation and accumulate reactive oxygen species. Plant Phys. *151*, 1790–1801.

Kawade, K., Horiguchi, G., and Tsukaya, H. (2010). Non-cell-autonomously coordinated organ size regulation in leaf development. Development *137*, 4221–4227.

Kawade, K., Horiguchi, G., Usami, T., Hirai, M.Y., and Tsukaya, H. (2013). ANGUSTIFOLIA3 signaling coordinates proliferation between clonally distinct cells in leaves. Curr. Biol. *23*, 788–792.

Kennaway, R., Coen, E.S., Green, A., and Bangham, A. (2011). Generation of diverse biological forms through combinatorial interactions between tissue polarity and growth. PLoS Comput. Biol. *7*, e1002071.

Kierzkowski, D., Nakayama, N., Routier-Kierzkowska, A.-L., Weber, A., Bayer, E., Schorderet, M., Reinhardt, D., Kuhlemeier, C., and Smith, R.S. (2012). Elastic domains regulate growth and organogenesis in the plant shoot apical meristem. Science *335*, 1096–1099.

Kim, J.H., and Kende, H. (2004). A transcriptional coactivator, AtGIF1, is involved in regulating leaf growth and morphology in *Arabidopsis*. Proc. Natl. Acad. Sci. USA *101*, 13374–13379.

Kolodziejczak, M., Gibala, M., Urantowka, A., and Janska, H. (2007). The significance of *Arabidopsis* AAA proteases for activity and assembly/stability of mitochondrial OXPHOS complexes. Physiol. Plant *129*, 135–142.

Kuchen, E.E., Fox, S., Barbier de Reuille, P., Kennaway, R., Bensmihen, S., Avondo, J., Calder, G.M., Southam, P., Robinson, S., Bangham, A., et al. (2012). Generation of leaf shape through early patterns of growth and tissue polarity. Science *335*, 1092–1096.

Kussell, E., and Leibler, S. (2005). Phenotypic diversity, population growth, and information in fluctuating environments. Science *309*, 2075–2078.

Kutschera, U., and Niklas, K.J. (2007). The epidermal-growth-control theory of stem elongation: an old and a new perspective. J. Plant Physiol. *164*, 1395–1409.

Lander, A.D. (2011). Pattern, growth, and control. Cell *144*, 955–969.

Levy, S.F., and Siegal, M.L. (2008). Network hubs buffer environmental variation in *Saccharomyces cerevisiae*. PLoS Biol. *6*, e264.

Little, S.C., Tikhonov, M., and Gregor, T. (2013). Precise developmental gene expression arises from globally stochastic transcriptional activity. Cell *154*, 789–800.

Lu, D., Wang, T., Persson, S., Mueller-Roeber, B., and Schippers, J.H.M. (2014). Transcriptional control of ROS homeostasis by KUODA1 regulates cell expansion during leaf development. Nat. Commun. *5*, 1–9.

Lukowitz, W., Gillmor, C.S., and Scheible, W.R. (2000). Positional cloning in *Arabidopsis*. Why it feels good to have a genome initiative working for you. Plant Phys. *123*, 795–805.

Martin, A.C., Kaschube, M., and Wieschaus, E.F. (2009). Pulsed contractions of an actin-myosin network drive apical constriction. Nature *457*, 495–499.

Meyer, H.M., and Roeder, A.H.K. (2014). Stochasticity in plant cellular growth and patterning. Front. Plant Sci. *5*, 420.

Mhamdi, A., Queval, G., Chaouch, S., Vanderauwera, S., Van Breusegem, F., and Noctor, G. (2010). Catalase function in plants: a focus on *Arabidopsis* mutants as stress-mimic models. J. Exp. Bot. *61*, 4197–4220.

Milani, P., Gholamirad, M., Traas, J., Arnéodo, A., Boudaoud, A., Argoul, F., and Hamant, O. (2011). In vivo analysis of local wall stiffness at the shoot apical meristem in *Arabidopsis* using atomic force microscopy. Plant J. *67*, 1116–1123.

Mittler, R., Vanderauwera, S., Gollery, M., and Van Breusegem, F. (2004). Reactive oxygen gene network of plants. Trends Plant Sci. *9*, 490–498.

Mittler, R., Vanderauwera, S., Suzuki, N., Miller, G., Tognetti, V.B., Vandepoele, K., Gollery, M., Shulaev, V., and Van Breusegem, F. (2011). ROS signaling: the new wave? Trends Plant Sci. *16*, 300–309.

Mizukami, Y. (2001). A matter of size: developmental control of organ size in plants. Curr. Opin. Plant Biol. *4*, 533–539.

Mizukami, Y., and Fischer, R.L. (2000). Plant organ size control: *AINTEGUMENTA* regulates growth and cell numbers during organogenesis. Proc. Natl. Acad. Sci. USA *97*, 942–947.

Montagne, J., Stewart, M.J., Stocker, H., Hafen, E., Kozma, S.C., and Thomas, G. (1999). *Drosophila* S6 kinase: a regulator of cell size. Science *285*, 2126–2129.

Nath, U., Crawford, B.C.W., Carpenter, R., and Coen, E.S. (2003). Genetic control of surface curvature. Science *299*, 1404–1407.

Neufeld, T.P., la Cruz de, A.F., Johnston, L.A., and Edgar, B.A. (1998). Coordination of growth and cell division in the *Drosophila* wing. Cell *93*, 1183–1193.

Ohno, C.K., Reddy, G.V., Heisler, M.G.B., and Meyerowitz, E.M. (2004). The *Arabidopsis JAGGED* gene encodes a zinc finger protein that promotes leaf tissue development. Development *131*, 1111–1122.

Owusu-Ansah, E., Yavari, A., Mandal, S., and Banerjee, U. (2008). Distinct mitochondrial retrograde signals control the G1-S cell cycle checkpoint. Nat. Genet. *40*, 356–361.

Palatnik, J.F., Allen, E., Wu, X., Schommer, C., Schwab, R., Carrington, J.C., and Weigel, D. (2003). Control of leaf morphogenesis by microRNAs. Nature *425*, 257–263.

Peaucelle, A., Louvet, R., Johansen, J.N., Höfte, H., Laufs, P., Pelloux, J., and Mouille, G. (2008). *Arabidopsis* phyllotaxis is controlled by the methyl-esterification status of cell-wall pectins. Curr. Biol. *18*, 1943–1948.

Peaucelle, A., Braybrook, S.A., Le Guillou, L., Bron, E., Kuhlemeier, C., and Höfte, H. (2011). Pectin-induced changes in cell wall mechanics underlie organ initiation in *Arabidopsis*. Curr. Biol. *21*, 1720–1726.

Perez, I.B., and Brown, P.J. (2014). The role of ROS signaling in cross-tolerance: from model to crop. Front. Plant Sci. *5*, 754.

Powell, A.E., and Lenhard, M. (2012). Control of organ size in plants. Curr. Biol. *22*, R360–R367.

Pulliam, D.A., Bhattacharya, A., and Van Remmen, H. (2013). Mitochondrial dysfunction in aging and longevity: a causal or protective role? Antioxid. Redox Signal. *19*, 1373–1387.

Qu, X., Chatty, P.R., and Roeder, A.H.K. (2014). Endomembrane trafficking protein SEC24A regulates cell size patterning in *Arabidopsis*. Plant Phys. *166*, 1877–1890.

Ralph, J., Bunzel, M., Marita, J.M., Hatfield, R.D., Lu, F., Kim, H., Schatz, P.F., Grabber, J.H., and Steinhart, H. (2004). Peroxidase-dependent cross-linking reactions of *p*-hydroxycinnamates in plant cell walls. Phytochem. Rev. *3*, 79–96.

Ren, M.M., Qiu, S.S., Venglat, P.P., Xiang, D.D., Feng, L.L., Selvaraj, G.G., and Datla, R.R. (2011). Target of rapamycin regulates development and ribosomal RNA expression through kinase domain in *Arabidopsis*. Plant Phys. *155*, 1367–1382.

Reyt, G., Boudouf, S., Boucherez, J., Gaymard, F., and Briat, J.-F. (2015). Iron- and ferritin-dependent reactive oxygen species distribution: impact on *Arabidopsis* root system architecture. Mol. Plant *8*, 439–453.

Rinott, R., Jaimovich, A., and Friedman, N. (2011). Exploring transcription regulation through cell-to-cell variability. Proc. Natl. Acad. Sci. USA *108*, 6329–6334.

Rodríguez, A.A., Grunberg, K.A., and Taleisnik, E.L. (2002). Reactive oxygen species in the elongation zone of maize leaves are necessary for leaf extension. Plant Phys. *129*, 1627–1632.

Roeder, A.H.K., Chickarmane, V., Cunha, A., Obara, B., Manjunath, B.S., and Meyerowitz, E.M. (2010). Variability in the control of cell division underlies sepal epidermal patterning in *Arabidopsis thaliana*. PLoS Biol. *8*, e1000367.

Roeder, A.H.K., Tarr, P.T., Tobin, C., Zhang, X., Chickarmane, V., Cunha, A., and Meyerowitz, E.M. (2011). Computational morphodynamics of plants: integrating development over space and time. Nat. Rev. Mol. Cell Biol. *12*, 265–273.

Roeder, A.H.K., Cunha, A., Ohno, C.K., and Meyerowitz, E.M. (2012). Cell cycle regulates cell type in the *Arabidopsis* sepal. Development *139*, 4416–4427.

Russo, T., Zambrano, N., Esposito, F., Ammendola, R., Cimino, F., Fiscella, M., Jackman, J., O'Connor, P.M., Anderson, C.W., and Appella, E. (1995). A P53-independent pathway for activation of WAF1/CIP1 expression following oxidative stress. J. Biol. Chem. *270*, 29386–29391.

Sakamoto, W. (2003). Coordinated regulation and complex formation of YELLOW VARIEGATED1 and YELLOW VARIEGATED2, chloroplastic FtsH metalloproteases involved in the repair cycle of photosystem II in *Arabidopsis* thylakoid membranes. Plant Cell *15*, 2843–2855.

Sassi, M., Ali, O., Boudon, F., Cloarec, G., Abad, U., Cellier, C., Chen, X., Gilles, B., Milani, P., Friml, J., et al. (2014). An auxin-mediated shift toward growth isotropy promotes organ formation at the shoot meristem in *Arabidopsis*. Curr. Biol. *24*, 2335–2342.

Sauret-Güeto, S., Schiessl, K., Bangham, A., Sablowski, R., and Coen, E.S. (2013). *JAGGED* controls *Arabidopsis* petal growth and shape by interacting with a divergent polarity field. PLoS Biol. *11*, e1001550.

Savaldi-Goldstein, S., Peto, C., and Chory, J. (2007). The epidermis both drives and restricts plant shoot growth. Nature *446*, 199–202.

Schiessl, K., Kausika, S., Southam, P., Bush, M., and Sablowski, R. (2012). JAGGED Controls growth anisotropy and coordination between cell size and cell cycle during plant organogenesis. Curr. Biol. *22*, 1739–1746.

Schopfer, P. (2001). Hydroxyl radical-induced cell-wall loosening in vitro and in vivo: implications for the control of elongation growth. Plant J. *28*, 679–688.

Schweikert, C., Liszkay, A., and Schopfer, P. (2000). Scission of polysaccharides by peroxidase-generated hydroxyl radicals. Phytochemistry *53*, 565–570.

Singh, A.M., Chappell, J., Trost, R., Lin, L., Wang, T., Tang, J., Wu, H., Zhao, S., Jin, P., and Dalton, S. (2013). Cell-cycle control of developmentally regulated transcription factors accounts for heterogeneity in human pluripotent cells. Stem Cell Rep. *1*, 532–544.

Smyth, D.R., Bowman, J.L., and Meyerowitz, E.M. (1990). Early flower development in *Arabidopsis*. Plant Cell *2*, 755–767.

Somerville, C., Bauer, S., Brininstool, G., Facette, M., Hamann, T., Milne, J., Osborne, E., Paredez, A., Persson, S., Raab, T., et al. (2004). Toward a systems approach to understanding plant cell walls. Science *306*, 2206–2211.

Tauriello, G., Meyer, H.M., Smith, R.S., Koumoutsakos, P., and Roeder, A.H.K. (2015). Variability and constancy in cellular growth of *Arabidopsis* sepals. Plant Phys. *169*, 2342–2358.

Thorsness, P.E., and Fox, T.D. (1993). Nuclear mutations in *Saccharomyces cerevisiae* that affect the escape of DNA from mitochondria to the nucleus. Genetics *134*, 21–28.

Thorsness, P.E., White, K.H., and Fox, T.D. (1993). Inactivation of *YME1*, a member of the *ftsH-SEC18-PAS1-CDC48* family of putative ATPase-encoding genes, causes increased escape of DNA from mitochondria in *Saccharomyces cerevisiae*. Mol. Cell Biol. *13*, 5418–5426.

Tsukagoshi, H., Busch, W., and Benfey, P.N. (2010). Transcriptional regulation of ROS controls transition from proliferation to differentiation in the root. Cell *143*, 606–616.

Tumaneng, K., Russell, R.C., and Guan, K.-L. (2012). Organ size control by Hippo and TOR pathways. Curr. Biol. *22*, R368–R379.

Urantowka, A., Knorpp, C., Olczak, T., Kolodziejczak, M., and Janska, H. (2005). Plant mitochondria contain at least two *i*-AAA-like complexes. Plant Mol. Biol. *59*, 239–252.

Uyttewaal, M., Burian, A., Alim, K., Landrein, B., Borowska-Wykręt, D., Dedieu, A., Peaucelle, A., Ludynia, M., Traas, J., Boudaoud, A., et al. (2012). Mechanical stress acts via katanin to amplify differences in growth rate between adjacent cells in *Arabidopsis*. Cell *149*, 439–451.

Vallejo, D.M., Juarez-Carreño, S., Bolivar, J., Morante, J., and Dominguez, M. (2015). A brain circuit that synchronizes growth and maturation revealed through Dilp8 binding to Lgr3. Science *350*, aac6767.

Vogel, G. (2013). Mysteries of development: how do organs know when they have reached the right size? Science *340*, 1156–1157.

Wagner, R., Aigner, H., Pružinská, A., Jänkänpää, H.J., Jansson, S., and Funk, C. (2011). Fitness analyses of *Arabidopsis thaliana* mutants depleted of FtsH metalloproteases and characterization of three FtsH6 deletion mutants exposed to high light stress, senescence and chilling. New Phytol. *191*, 449–458.

Weigmann, K., Cohen, S.M., and Lehner, C.F. (1997). Cell cycle progression, growth and patterning in imaginal discs despite inhibition of cell division after inactivation of *Drosophila* Cdc2 kinase. Development *124*, 3555–3563.

White, D.W.R. (2006). *PEAPOD* regulates lamina size and curvature in *Arabidopsis*. Proc. Natl. Acad. Sci. USA *103*, 13238–13243.

Williams, R.W. (2000). Mapping genes that modulate mouse brain development: a quantitative genetic approach. In Mouse Brain Development, A.M. Goffinet and P. Rakic, eds. (Berlin, Heidelberg: Springer), pp. 21–49.

Wolf, L., Silander, O.K., and van Nimwegen, E.J. (2015). Expression noise facilitates the evolution of gene regulation. eLife *4*, e05856.

Wolpert, L. (2010). Arms and the man: the problem of symmetric growth. PLoS Biol. *8*, e1000477.

Xia, X.-J., Zhou, Y.-H., Shi, K., Zhou, J., Foyer, C.H., and Yu, J.-Q. (2015). Interplay between reactive oxygen species and hormones in the control of plant development and stress tolerance. J. Exp. Bot. *66*, 2839–2856.

Xue, J., Luo, D., Xu, D., Zeng, M., Cui, X., Li, L., and Huang, H. (2015). CCR1, an enzyme required for lignin biosynthesis in *Arabidopsis*, mediates cell proliferation exit for leaf development. Plant J. *83*, 375–387.

Yakubov, G.E., Bonilla, M.R., Chen, H., Doblin, M.S., Bacic, A., Gidley, M.J., and Stokes, J.R. (2016). Mapping nano-scale mechanical heterogeneity of primary plant cell walls. J. Exp. Bot. *67*, 2799–2816.

Zhang, C., Halsey, L.E., and Szymanski, D.B. (2011). The development and geometry of shape change in *Arabidopsis thaliana* cotyledon pavement cells. BMC Plant Biol. *11*, 27.

Zhang, S., Zhang, D., and Yang, C. (2014). *AtFtsH4* perturbs the mitochondrial respiratory chain complexes and auxin homeostasis in *Arabidopsis*. Plant Signal. Behav. *9*, e29709.